



Raytheon

SEA SURFACE TEMPERATURE

VISIBLE/INFRARED IMAGER/RADIOMETER SUITE

ALGORITHM THEORETICAL BASIS DOCUMENT

Version 5: March 2002

Richard J. Sikorski
Shawn W. Miller
Peter S. Kealy

William Emery, Science Team Member
University of Colorado

RAYTHEON SYSTEMS COMPANY
Information Technology and Scientific Services
4400 Forbes Boulevard
Lanham, MD 20706

SBRS Document #: Y2386

EDR: SEA SURFACE TEMPERATURE

Doc No: Y2386

Version: 5

Revision: 3

	FUNCTION	NAME	SIGNATURE	DATE
Prepared By	EDR Developer	R. SIKORSKI		1/18/02
Approved By	Reviewer	P. KEALY		1/30/02
Approved By	Surface Temperature IPT Lead	R. SIKORSKI		2/11/02
Approved By	Chief Scientist	S. MILLER		2/15/02
Released By	Program Manager	P. KEALY		2/15/02

TABLE OF CONTENTS

	<u>Page</u>
LIST OF FIGURES	iii
LIST OF TABLES	vii
GLOSSARY OF ACRONYMS	ix
ABSTRACT	xi
1.0 INTRODUCTION	1
1.1 PURPOSE	1
1.2 SCOPE	1
1.3 VIIRS DOCUMENTS	1
1.4 REVISIONS	1
2.0 EXPERIMENT OVERVIEW	3
2.1 OBJECTIVES OF SEA SURFACE TEMPERATURE RETRIEVALS	3
2.2 INSTRUMENT CHARACTERISTICS	4
2.3 SST RETRIEVAL STRATEGY	6
3.0 ALGORITHM DESCRIPTION	9
3.1 PROCESSING OUTLINE	9
3.2 ALGORITHM INPUT	10
3.2.1 VIIRS Data	10
3.2.2 Non-VIIRS Data	10
3.3 THEORETICAL DESCRIPTION OF SST RETRIEVAL	10
3.3.1 Physics of the Problem	10
3.3.2 Mathematical Description of the Algorithm	18
3.3.2.1 Regression Methods	18
3.3.2.2 Enhancement of the dual split window algorithm	18
3.3.3 Algorithm Output	22
3.3.4 Variance and Uncertainty Estimate	22

3.4	ALGORITHM SENSITIVITY STUDIES.....	23
3.4.1	Test Data Sets.....	23
3.4.2	Sensor Noise Effects	27
3.4.3	Water Vapor Effects.....	28
3.4.4	Calibration Errors.....	31
3.4.5	Band-to-Band Registration and Modulation Transfer Function	42
3.5	PRACTICAL CONSIDERATIONS.....	50
3.5.1	Numerical Computation Consideration	50
3.5.2	Programming and Procedural Considerations.....	50
3.5.3	Configuration of Retrievals.....	50
3.5.4	Quality Assessment and Diagnostics	50
3.5.5	Exception Handling.....	52
3.6	ALGORITHM VALIDATION.....	52
3.6.1	Pre-Launch Validation	52
3.6.2	Post-Launch Calibration and Validation.....	53
3.7	ALGORITHM DEVELOPMENT SCHEDULE	55
4.0	ASSUMPTIONS AND LIMITATIONS	57
4.1	SENSOR PERFORMANCE.....	57
4.2	P ³ I.....	57
4.2.1	Aerosol Correction by AOT and Aerosol Type	57
4.2.2	Derivation of Bulk SST from Skin SST	63
4.2.3	Emissivity Correction	65
4.2.4	Iterative Water Vapor Correction.....	66
4.2.5	Physical SST Retrieval.....	66
4.2.6	Extended Air mass Classification	66
5.0	REFERENCES	67

LIST OF FIGURES

	<u>Page</u>
Figure 1. IR radiance at satellite height for five standard atmospheres simulated by MODTRAN.....	5
Figure 2. Atmospheric transmittances for five atmospheres.....	5
Figure 3. SST high level flowchart: Statistical Method.....	9
Figure 4. Water vapor vs. sea surface temperature distribution.....	11
Figure 5. Transmittance vs. SST.....	12
Figure 6. Transmittance vs. total column water vapor over ocean.....	12
Figure 7. Temperature deficits ($T_{\text{surface}} - T_{\text{brightness}}$) vs. total column water vapor distribution.....	13
Figure 8. The relationship between temperature deficits at AVHRR channel 4 and channel 5 from observations.....	15
Figure 9. The relationship between temperature deficits at AVHRR channel 4 and channel 5 from simulation of a transmittance model.....	16
Figure 10. The relationship between temperature deficits at AVHRR channel 4 and channel 5 from MODTRAN simulations.....	17
Figure 11. TRMM VIRS channel 3 brightness temperature ($3.7\ \mu\text{m}$), channel 1 ($0.66\ \mu\text{m}$) reflectance, Channel 4 ($11\ \mu\text{m}$) brightness temperature, and channel 5 ($12\ \mu\text{m}$) brightness temperature.....	19
Figure 12. Air mass classification diagram – step 1 (warm/cold).....	20
Figure 13. Air mass classification diagram –step 2 (moist/dry).....	20
Figure 14. SST bias comparison between unimproved VIIRS baseline dual split window algorithm and the algorithm with air mass classification enhancements.....	21
Figure 15. The total uncertainty with all error sources including SBRS calibration perturbation, specified and predicted sensor noises, for the VIIRS baseline dual split window algorithm. (a) Uncertainty from the specified sensor noise, (b) Uncertainty from the predicted sensor noise.....	22
Figure 16. (a) Range of the 299 ship-observed SSTs. (b) Difference between true SST and retrieved SST. Green line: daytime. Black line: nighttime.....	24

Figure 17a. Global SST. b. Retrieved SST. c. The difference between global and retrieved SSTs	25
Figure 18a. Observed 1 km SST. b. Retrieved SST using equation derived from 25% of the observed data. c. Retrieved SST using equation derived from global NCEP data. The noise was added by using the SBRS sensor noise model 3.....	26
Figure 19. Dual split window (3.7, 4.0, 10.8, 12.0 μm) SST precision as function of satellite viewing angle and SST range. (a) Daytime. (b) Nighttime.....	28
Figure 21. The SST retrieval error distribution vs. sensor viewing angle and total column water vapor for sensor noise model 3 for the VIIRS baseline dual split window algorithm. Upper Panel (Precision), Middle (Accuracy), Bottom (uncertainty)	29
Figure 22. The SST retrieval error distribution vs. sensor viewing angle and total column water vapor for sensor noise model 3 for the VIIRS fallback split window algorithm. Upper Panel (Precision), Middle (Accuracy), Bottom (uncertainty)	30
Figure 23. Dual split window SST accuracy relevant to calibration error.....	32
Figure 24. Split window SST accuracy relevant to calibration error.....	32
Figure 25. Uncertainties for the VIIRS 10.8 μm band.....	34
Figure 26. ρ_{ev} as a function of satellite viewing angle for the VIIRS 10.8 μm band.	35
Figure 27. VIIRS baseline dual split window SST accuracy derived from NCEP data, assuming errors for all bands are correlated.....	36
Figure 28. VIIRS baseline dual split window SST accuracy derived from NCEP data, assuming errors for all bands are not correlated.	37
Figure 29. VIIRS fallback split window SST accuracy derived from NCEP data, assuming errors for all bands are correlated.....	38
Figure 30. VIIRS fallback split window SST accuracy derived from NCEP data, assuming errors for all bands are not correlated.....	39
Figure 31. SST RMS accuracy from SBRS 32 perturbation.....	40
Figure 32. (a) SST RMS accuracy, (b)accuracy with knowledge of calibration for VIIRS baseline dual split window algorithm, (c) RMS accuracy with knowledge of calibration for VIIRS fallback split window algorithm, and (d) RMS accuracy without knowledge of calibration of VIIRS baseline dual split window algorithm.	41

Figure 33. SST precision relevant to BBR. The misregistration ranges from 0.0 to 0.5 of the pixel area.	42
Figure 34. SST fields of Test Scene I (Open Ocean Scene).....	43
Figure 35. SST fields of Test Scene II (Gulf Stream off Florida).....	43
Figure 36. VIIRS baseline dual split window MTF results from open ocean scene.	44
Figure 37. VIIRS baseline dual split window MTF results from Gulf Stream Scene.....	45
Figure 38. VIIRS fallback split window MTF results from Gulf Stream Scene.....	46
Figure 39. The combined effects of BBR and MTF on the VIIRS baseline dual split window SST algorithm for open ocean scene.	47
Figure 40. The combined effects of BBR and MTF on VIIRS baseline dual split window SST algorithm for Gulf Stream scene.	48
Figure 41. The combined effects of BBR and MTF on split window SST algorithm for Gulf Stream scene.	49
Figure 42. Daytime SST accuracy as a function of optical thickness in testing data.....	58
Figure 43. Nighttime SST accuracy as a function of optical thickness in testing data.	58
Figure 44. (a) SST precision as a function of AOT. (b) Nighttime SST precision as a function of AOT.	59
Figure 45. SST accuracy as a function of optical thickness and aerosol heights.	60
Figure 46. (a) AOT distribution. (b) Retrieved SST bias without aerosol correction. (c) SST bias after aerosol correction to brightness temperature. (d) SST bias after aerosol correction.	61
Figure 47. (a) Cloud type distribution in the simulation. (b) SST bias without the consideration of aerosol type. (c) After correction to both of AOT and the aerosol type.....	63
Figure 48. Bulk-skin SST difference (upper panel), and the surface wind field at the same time (lower panel).....	65

LIST OF TABLES

	<u>Page</u>
Table 1. Channel Characteristics of Satellite-borne IR Radiometers	6
Table 2. Sensor Performance for Sea Surface Temperature	6
Table 3. Comparisons of the dual split window SST Precision	27
Table 4. VIIRS Fractional Radiance Uncertainty	33
Table 5. Scene Temperature Uncertainty	33
Table 6. VIIRS 4-Byte SST Flags	51

GLOSSARY OF ACRONYMS

AOI	Angle of Incidence
AOT	Aerosol Optical Thickness
ATBD	Algorithm Theoretical Basis Document
ATSR	Along Track Scanning Radiometer
AVHRR	Advanced Very High Resolution Radiometer
BBR	Band-to-Band Registration
BTM _n	VIIRS Emissive Band, where n = 12, 13, 14, 15, or 16
CAIV	Cost As an Independent Variable
DCS	Data Collection System on NPOESS
ECMWF	European Center for Medium-Range Weather Forecast
EDR	Environmental Data Record
EOS	Edge of Scan
GLI	Global Imager
GSD	Ground Sample Distance
HCS	Horizontal Cell Size
IPO	Integrated Program Office
IR	Infrared
LOWTRAN	Low-resolution Transmission Model
LWIR	Longwave Infrared
MCSST	Multi-Channel Regression Method SST
MODIS	Moderate Resolution Imaging Spectroradiometer
MODTRAN	Moderate Resolution Transmission Model
MOSART	Moderate Spectral Atmospheric Radiance and Transmittance
MTF	Modulation Transfer Function
MWIR	Midwave Infrared
NCEP	National Centers for Environment Prediction
NEdT	Noise-Equivalent Temperature Difference
NESDIS	National Environmental Satellite, Data and Information Service
NPOESS	National Polar-orbiting Operational Environmental Satellite System
OCTS	Ocean Color and Temperature Scanner

P ³ I	Pre-Planned Product Improvement
PW	Precipitable Water
RMn	VIIRS Reflective Bands, where n = 5, 7, or 9
RMS	Root Mean Square
RVS	Response Versus Scan Angle
SBRS	Santa Barbara Remote Sensing
SRD	Sensor Requirements Document
SST	Sea Surface Temperature
TIR	Thermal Infrared
TOA	Top of Atmosphere
TRMM	Tropical Rainfall Measuring Mission
VIIRS	Visible/Infrared Imager/Radiometer Suite
VIRS	TRMM Visible Infrared Scanner

ABSTRACT

This is the Algorithm Theoretical Basis Document (ATBD) for Sea Surface Temperature (SST) retrieval from Infrared (IR) signals received by the National Polar-orbiting Operational Environmental Satellite System (NPOESS) Visible/Infrared Imager/Radiometer Suite (VIIRS). SST is an input variable for other VIIRS products such as net heat flux. The SST Unit will produce the VIIRS SST Environmental Data Record (EDR).

This document describes the theoretical basis of the SST algorithms, which have been developed by the NPOESS algorithm team. These algorithms were derived from the atmospheric water vapor correction SST algorithm, which uses two or more IR-bands in an atmospheric window to correct water vapor, and is a heritage algorithm of the Advanced Very High Resolution Radiometer (AVHRR), the Along Track Scanning Radiometer (ATSR), and the Moderate Resolution Imaging Spectroradiometer (MODIS). The VIIRS baseline algorithm employs a dual split window (3.7, 4.0, 10.8, and 12 μm) algorithm to retrieve both skin and bulk SST, in both daytime and nighttime. During sun glint conditions, the VIIRS fallback split window (10.8 and 12.0 μm) algorithm is used. The algorithms include satellite zenith angle correction and daytime solar correction.

The results from VIIRS testbed indicate a successful solar correction in the daytime by using a split window in Midwave IR (MWIR) window. The VIIRS baseline dual split window algorithm achieves SST precision of 0.3 K in both daytime and nighttime. This precision is further improved to 0.25 K by an air mass classification technique. The VIIRS SST EDR requires a 0.2 K measurement accuracy and 0.5 K measurement uncertainty, which yields a precision requirement of about 0.45 K. VIIRS Precipitable Water (PW) product will contribute to the SST air mass classifications.

Major constraints for the surface temperature algorithms are instrument band selection, instrument Noise-Equivalent Temperature Difference (NE Δ T) for each band, instrument calibration, and the availability and quality of the pre-launch and post-launch surface calibration/validation observations. The performance of the VIIRS SST algorithm are be strongly dependent on the establishment of the match-up database.

1.0 INTRODUCTION

1.1 PURPOSE

This document describes the theoretical basis of the SST algorithm, for retrieval of the VIIRS SST Environmental Data Record (EDR). Algorithm validation, algorithm sensitivity, constraints, limitations, and assumptions are also discussed.

1.2 SCOPE

The SST algorithms described in this document will be used routinely to retrieve both skin and bulk SSTs from VIIRS measurements. P³I efforts may result in further enhancements to the current operational algorithms.

The next section provides a brief overview. Descriptions of the algorithm are presented in Section 3, along with discussions of algorithm sensitivity to various physical parameters. Calibration and validation are also discussed in Section 3. Constraints, assumptions, and limitations are identified in Section 4.

1.3 VIIRS DOCUMENTS

Reference to VIIRS documents are indicated by a number in italicized brackets, e.g., [*V-1*].

1.4 REVISIONS

This is the fifth version of the document, dated January 2002. Most of the revisions in this document are in response to a set of comments and questions received from the VIIRS Operational Algorithm Team. In addition, flowdown and development details were reduced in this version, and can be found in version four. Substantial contributions to prior versions of this document, including algorithm development, were made by Yimin Ji, Philip E. Ardanuy, Donglian Sun, Quanhua Liu, and Wenli Yang.

2.0 EXPERIMENT OVERVIEW

2.1 OBJECTIVES OF SEA SURFACE TEMPERATURE RETRIEVALS

With about 70% of the Earth's surface covered by ocean, the variability of sea surface temperatures has a significant socio-economic impact. For example, slow variations of SST over the tropics and subtropics can substantially change the planetary atmospheric flow and are the dominant factors in global and regional climate changes. Variations of SST of less than 1 K can occur anywhere over the ocean. However, variations greater than 1 K over a large area usually occur only during El Niño events. In some El Niño events, the SST over the eastern equatorial Pacific may be 4-5 K higher than the climate mean. SST is also a good indicator of global warming. However, ground truth data over the vast oceans are limited. Therefore, satellite-based SST measurements combined with ground truth data have been a major source of high resolution SST data (Reynolds, 1988; Reynolds and Smith, 1994). Currently, the 14 km resolution weekly merged SSTs are used for operational weather forecasting in North America. Weekly merged SST products have also been used in climate simulations to understand the mechanisms of interannual and intraseasonal climate variability over Asia and America (e.g., Ji and Vernekar, 1997).

The accuracy of satellite SST determination has improved significantly since the development of radiometers with two or more atmospheric window channels within MWIR and LWIR windows (e.g., McClain *et al.*, 1983). The fundamental basis of multi-channel SST algorithms is the differential water vapor absorption in the various atmospheric window regions of the spectrum. The current satellite multi-channel SST algorithm can permit global SST retrievals on space scales of 8 km with a root mean square error ~ 0.3 K (Kearns *et al.*, 2000; McClain *et al.*, 1985; Barton *et al.*, 1993; Legeckis and Zhu, 1997; and May *et al.*, 1998). MODIS measurement accuracy requirement for SST is 0.35 K (Brown and Minnett, 1996). The current operational Multi-Channel Regression Method SST (MCSST) and the MODIS SST algorithms are statistical methods. These methods, which combine the satellite observation and *in situ* observation, have proven to be very successful in producing reliable global SST data sets. The current operational SST retrieval methods are based on two windows within the 10-13 μm interval in the daytime and an additional window within the 3.5-4.2 μm interval in the nighttime. Some research studies also used water vapor information in the statistical method (e.g., Emery *et al.*, 1994). Although physical retrievals have not been used for operational SST retrieval due to the large computational requirement and possible instability, they are promising methods for improving the retrieval precision. Physical retrievals need at least three bands to obtain sufficient information for the forward model.

Although it is widely accepted that IR sensors measure radiance from only the skin of the ocean, oceanographers are more interested in SSTs for the upper meters of the oceans, commonly referred to as bulk temperature (Schluessel *et al.*, 1990). This interest in the bulk temperature has led to the practice of calibrating satellite-derived SSTs with *in situ* bulk SST measured by ocean buoys. The difference between skin and bulk temperatures contributes an added level of uncertainty to the satellite SST retrieval. The relationship between skin and bulk SSTs has been investigated by a number of scientists (e. g., Schluessel *et al.*, 1990). Currently, the AVHRR SST is calibrated to bulk SST, while the ATSR measures the skin temperature (Zavody *et al.*,

1995). MODIS SST retrieval is a follow-up to AVHRR SST algorithm (Brown and Minnett, 1996), but is a skin temperature product.

The ATSR retrieval method is a physically based regression method. This method uses a line-by-line model to simulate the ATSR Top of Atmosphere (TOA) radiances and incorporates *in situ* skin SSTs with the simulated radiances. This method requires accurate models and highly qualified on-board calibration, as well as very low sensor noise.

The overall scientific objective of the VIIRS SST retrievals is to provide improved operational measurements of both skin and bulk SST fields by using statistical methods. The VIIRS SST EDR requires a 0.2 K measurement accuracy and a 0.5 K measurement uncertainty. These requirements exceed prior state-of-the-art operational results. However, these are minimum requirements from an environmental point of view. For example, a few tenths of a degree increase in global SST in a decade reflects a strong global warming trend. Over tropical oceans, atmospheric convective activities are sensitive to a small change of SSTs.

2.2 INSTRUMENT CHARACTERISTICS

The VIIRS MWIR and LWIR bands must be positioned to optimize their use for SST determination. Bands in the LWIR are usually located near the maximum Earth radiance. Influences of ozone and other atmospheric absorbers must be avoided. Figure 1 shows the MODTRAN simulated radiance at the height of the satellite for the Thermal IR (TIR) spectrum. There are two suitable regions for LWIR band selection: 8-9 μm and 10-13 μm . Three VIIRS LWIR bands are located in these two regions. Bands in the MWIR are usually located where the atmosphere is most transparent. Figure 2 shows the MODTRAN simulated atmospheric transmittance for five standard atmospheres. It shows that the 3.4-4.2 μm region is the most transparent atmospheric window. Two VIIRS MWIR bands are located in this window. In earlier versions of this ATBD, we investigated the effects of band location in the MWIR and LWIR windows. Those documents summarize the flowdown of the SRD requirements for the VIIRS SST to the present VIIRS IR band selection.

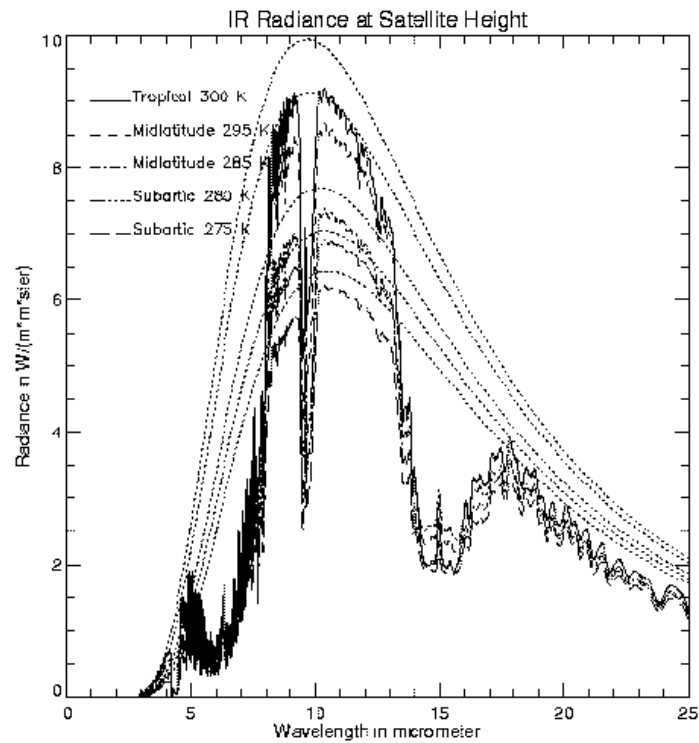


Figure 1. IR radiance at satellite height for five standard atmospheres simulated by MODTRAN.

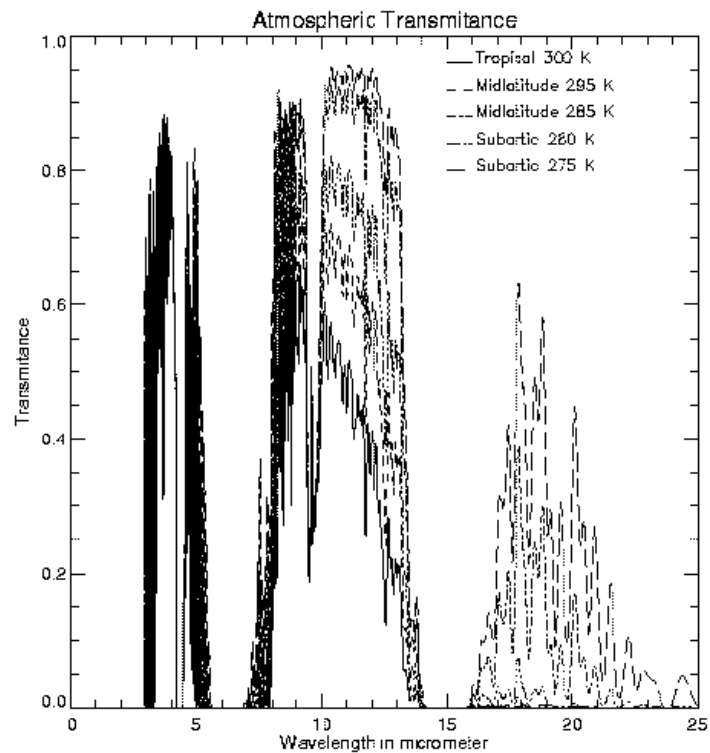


Figure 2. Atmospheric transmittances for five atmospheres.

The continuity requirement on SST derivation is also one of the factors for VIIRS band selection. Table 1 shows the bands chosen to retrieve SST for existing or proposed satellites.

Table 1. Channel Characteristics of Satellite-borne IR Radiometers

VIIRS baseline		MODIS		AVHRR		ATSR		OCTS		GLI	
$\lambda_{\mu m}$	NEdT K	$\lambda_{\mu m}$	NEdT K	$\lambda_{\mu m}$	NEdT K	$\lambda_{\mu m}$	NEdT K	$\lambda_{\mu m}$	NEdT K	$\lambda_{\mu m}$	NEdT K
3.7	0.065	3.75	0.05	3.75	0.12	3.7	0.019	3.7	0.15	3.715	<0.15
4.0	0.078	3.96	0.07								
		4.02	0.07								
10.8	0.038	11.03	0.05	10.5	0.12	10.8	0.028	10.8	0.15	10.8	<0.1
12.0	0.070	12.02	0.05	11.5	0.12	12	0.025	11.9	0.15	12	<0.1

To meet the VIIRS SST measurement requirements, the sensor must ensure very low radiometric noise for IR bands, especially the 10-12 μm window. Well-placed windows in the 3.6-4.2 μm are also important. The detailed specification of the current version of the sensor design are listed in Table 2.

Table 2. Sensor Performance for Sea Surface Temperature

		Native Sensor						Nadir						
Wave-length	Band Width	GSD				Ttyp	NEdT	Onboard Aggregation Factor		On ground Aggregation Factor		Effective Algorithm GSD		Effective Algorithm NEdT
		Nadir		EOS										
		Trk	Scn	Trk	Scn			Trk	Scn	Trk	Scn	Trk	Scn	
3.7	0.180	742	262	1094	617	300	0.065	1	3	1	1	742	786	0.038
4.0	0.155	742	262	1094	617	300	0.078	1	3	1	1	742	786	0.045
10.8	1.000	742	262	1094	617	300	0.038	1	3	1	1	742	786	0.022
12.0	0.950	742	262	1094	617	300	0.070	1	3	1	1	742	786	0.040

2.3 SST RETRIEVAL STRATEGY

Before SST retrievals are performed, a land/ocean mask is used to identify pixels to process. A cloud cover mask and a snow/ice mask are used to eliminate cloud-contaminated or snow/ice-

covered pixels. The SST algorithms are not run under confident-cloudy sky conditions; all other cloud conditions are flagged. The following sequence of SST retrieval activities is performed on all suitable pixels within a region. Solar zenith angle and viewing zenith angle are calculated and used to determine day or night retrieval and sun glint condition. The brightness temperatures are calculated for two MWIR bands (3.7 and 4.0 μm), if necessary, and for two LWIR bands (10.8 and 12.0 μm). Aerosol Optical Thickness (AOT) is evaluated, and an aerosol correction is applied to the brightness temperatures if needed. AOT, PW, and brightness temperature are evaluated for air mass classification. Appropriate sets of coefficients are loaded for both skin and bulk SST retrievals. Skin and bulk SST are both calculated using regression equations from the dual split window algorithm if possible, or from the fallback split window algorithm.

3.0 ALGORITHM DESCRIPTION

3.1 PROCESSING OUTLINE

The water vapor correction SST retrieval method is assisted initially by the establishment of global ancillary data sets and radiative transfer models. The coefficients are obtained through one time simulations and validated using ground observations. Figure 3 depicts the processing concept for SST retrieval.

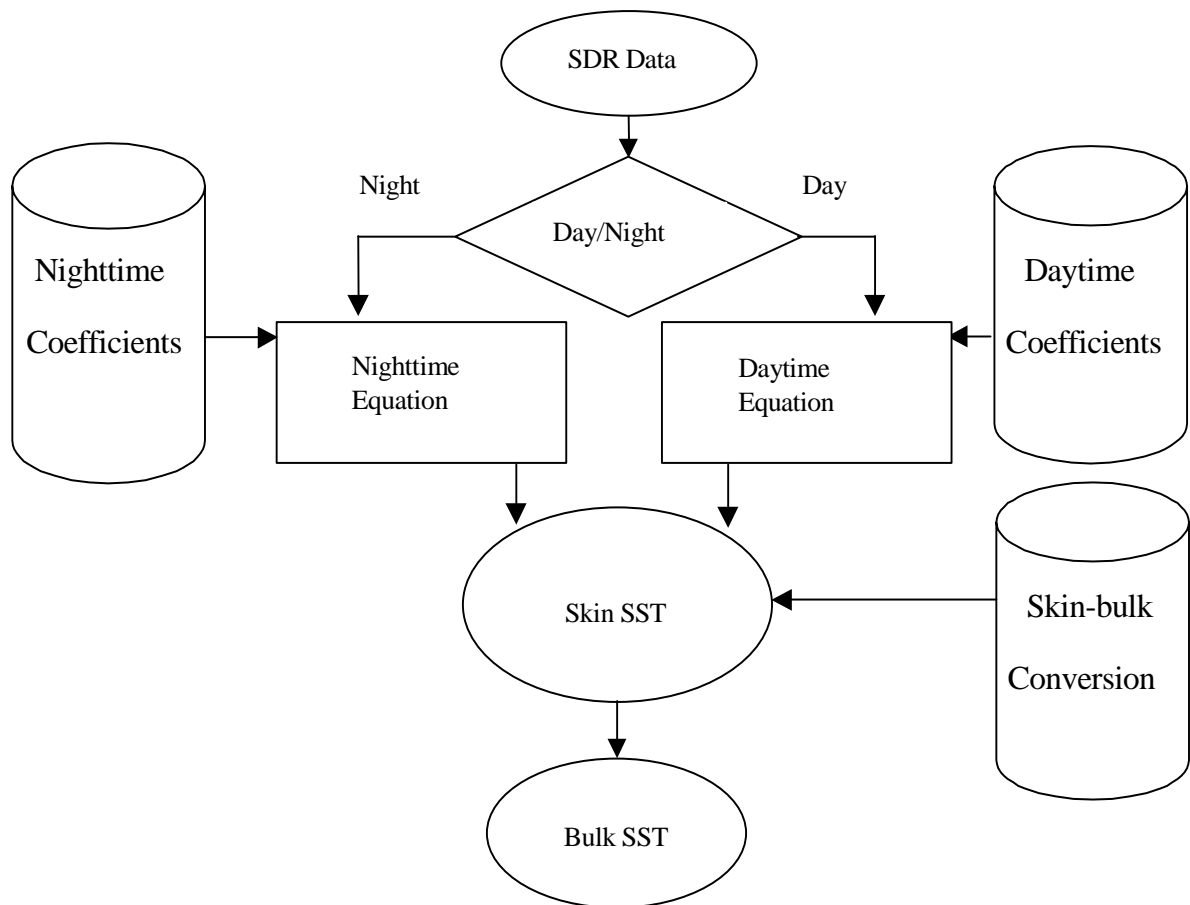


Figure 3. SST high level flowchart: Statistical Method.

3.2 ALGORITHM INPUT

3.2.1 VIIRS Data

Required inputs necessary for the SST retrieval from the VIIRS data stream are cloud mask, snow/ice mask, sun glint mask, TOA radiances (3.7, 4.0, 10.8, and 12.0 μm), PW, and AOT.

3.2.2 Non-VIIRS Data

Non-VIIRS ancillary data includes land/ocean mask.

3.3 THEORETICAL DESCRIPTION OF SST RETRIEVAL

3.3.1 Physics of the Problem

In clear sky conditions, the outgoing IR spectral radiance at the top of atmosphere can be represented by:

$$L(\lambda, \mu) = \tau(\lambda, \mu)\varepsilon(\lambda, \mu)B(\lambda, T_s) + L_a(\lambda, \mu) + L_s(\lambda, \mu, \mu_0, \varphi_0) + L_d(\lambda, \mu, \mu_0, \varphi_0) + L_r(\lambda, \mu, \mu_0, \varphi_0) \quad (1)$$

where τ is the transmissivity, ε the surface spectral emissivity, B the Plank function, L_a the thermal path radiance, L_s the path radiance resulting from scattering of solar radiation. L_d is the solar radiance and L_r the solar diffuse radiation and atmospheric thermal radiation reflected by the surface. $\mu = \cos(\theta)$, $\mu_0 = \cos(\psi)$, where θ is the satellite zenith angle, ψ the solar zenith angle. φ_0 is azimuth angle.

λ is the center wavelength of a narrow interval, because there is no way to measure the exact monochromatic signal as a continuous function of wavelength by satellite sensors. Equation 1 can be used in the 3–14 μm range. Complete calculation of atmospheric radiative transfer is necessary to determine the values of all terms on the right side. This equation has been used in many atmospheric radiation models including LOWTRAN (Kneizys *et al.*, 1983), MODTRAN (Berk *et al.*, 1989), and MOSART (Cornette *et al.*, 1994). The inversion of Equation 1 is not easy if the atmospheric conditions are unknown.

In order to infer the surface information, we should choose window channels with no or little atmospheric contribution. As shown in Figure 1, the wavelength between 3.5–4.2 μm , 8–9 μm , and 10–13 μm are some typical atmospheric windows. For a perfect window, the total atmospheric transmittance $\tau_0(\lambda, \mu)$ should be 1.0, the transmittance weighting function should be 0. However, as indicated in Figure 2, the transmittances at these windows are not 1.0 and are functions of atmospheric profiles. The main absorber for these windows is atmospheric water vapor.

In order to evaluate the water vapor contribution to various window channels, simulations were performed using 5139 profiles offered by the Integrated Program Office (IPO) over sea surface under clear sky conditions with MODTRAN 3.7. The following four window bands are

simulated: 3.7 μm , 10.8 μm (AVHRR channel 4), 12 μm (AVHRR channel 5), and 4.0 μm . Figure 4 shows the water vapor as a function of SST derived from these profiles. It shows much greater atmospheric water vapor concentrations over warmer SST above 285 K.

Figure 5 shows transmittance as a function of surface skin temperature. It indicates that the transmittances decrease significantly the LWIR channels, 10.8 μm and 12 μm , as SST becoming warmer (285–310 K). This explains why most existing split window algorithms using only 11 and 12 μm channels have larger errors at the warmer temperature above 285 K. The transmittances for the MWIR channels, 3.7 μm and 4.0 μm , are less sensitive to the surface skin temperature and are closer to 1.0 compared to those of LWIR channels. From this aspect, the MWIR 3.7 μm and 4.0 μm channels are better window channels than the LWIR 10.8 and 12 μm channels. The most stable channel is 4.0 μm . Figure 6 shows the transmittance vs. precipitable water distribution, it shows that the transmittance at the 4.0 μm channel changes very little with the column water vapor amount. While the transmittance at 3.7 μm channel has a linear relationship with the precipitable water, the transmittances at 10.8 and 12 μm decrease significantly as the water vapor increases, and the relationship is not linear. These results suggest that the MWIR window channels are needed for accurate retrieval of warmer surface temperatures.

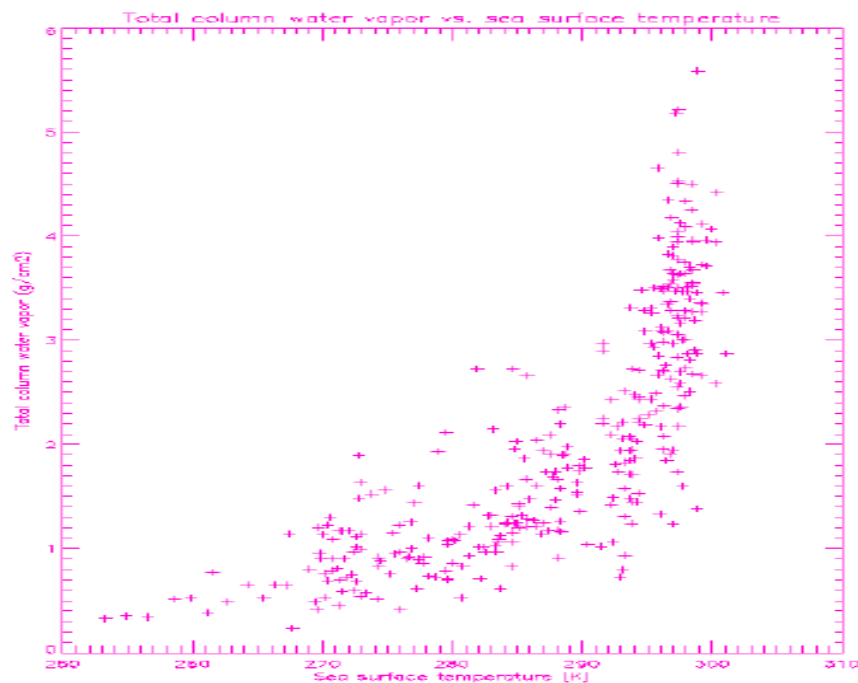


Figure 4. Water vapor vs. sea surface temperature distribution.

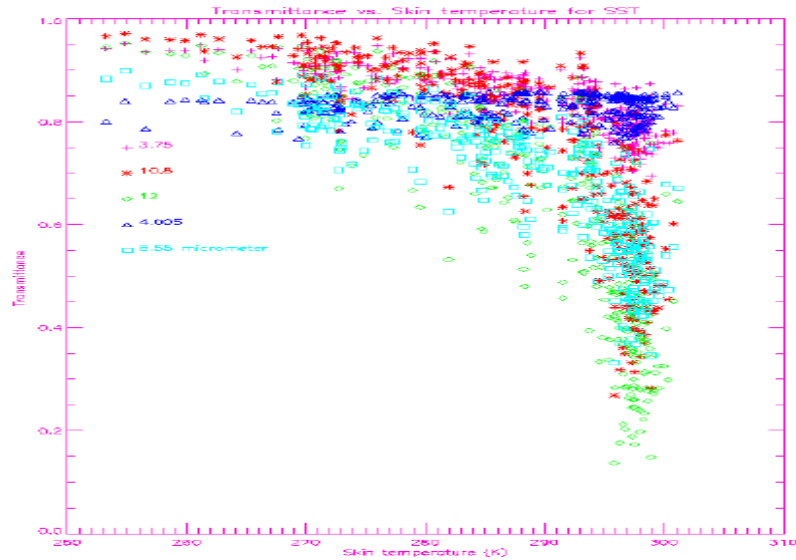


Figure 5. Transmittance vs. SST.

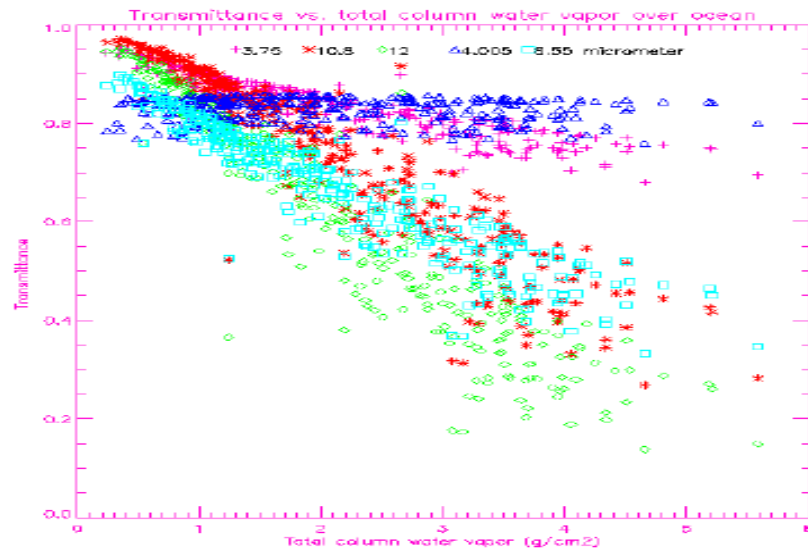


Figure 6. Transmittance vs. total column water vapor over ocean.

However, as shown in Figure 7, the temperature deficits ($T_{\text{surface}} - T_{\text{brightness}}$) in the LWIR window channels 10.8 and 12 μm are very stable, while the surface temperature can be much lower than the brightness temperature at MWIR channels 3.7 and 4.0 μm in daytime, sometimes by more than 10 degrees. This is because in the daytime, the MWIR channel contains both reflected solar radiation and radiation emitted by the surface and the atmosphere. Therefore, the solar contamination on MWIR channels must be corrected. The solar correction requires two or more MWIR bands.

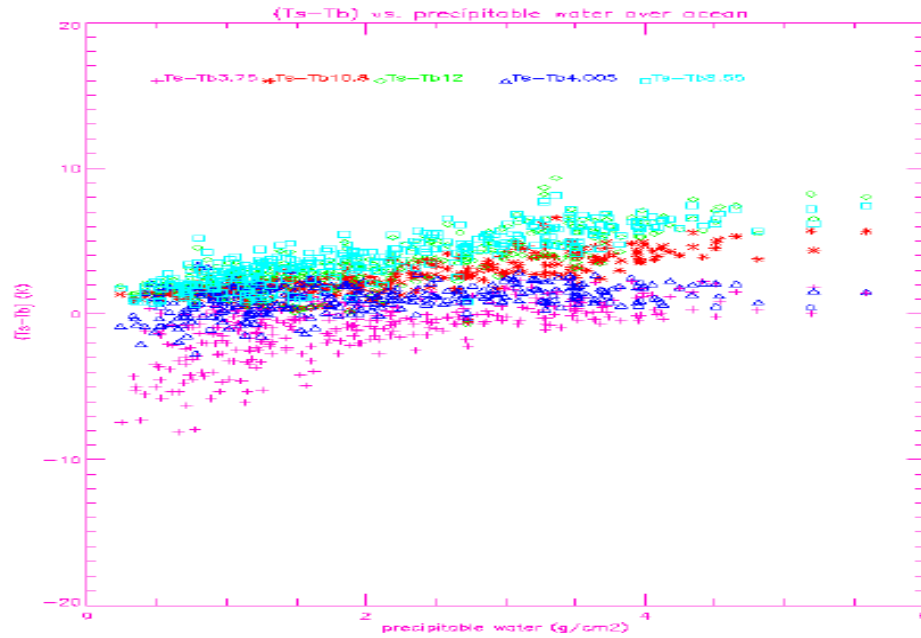


Figure 7. Temperature deficits (Tsurface-Tbrightness) vs. total column water vapor distribution.

It has been noted that satellite IR radiance can be corrected for atmospheric absorption in the atmospheric window spectrum by utilizing a split window technique. In the following discussion, we outline a theoretical basis for the split window method. In the LWIR window, this method can be extended to multi-band methods.

For LWIR bands, L_u , L_s and L_r are negligible. Therefore, only the first two terms on the right side of the above equation are important. In this case, if we ignore the change of emissivity over the ocean, the radiance error introduced by the atmosphere ΔL can be represented by:

$$\begin{aligned}
 \Delta L &= B(\lambda, T_s) - L(\lambda, \mu) = B(\lambda, T_s) - \tau(\lambda, \mu)B(\lambda, T_s) - L_a(\lambda, \mu) \\
 &= - \int_1^{\tau(\lambda, \mu)} B(\lambda, T_s) d\tau(\lambda, \mu, p) + \int_1^{\tau(\lambda, \mu)} B(\lambda, T_p) d\tau(\lambda, \mu, p) \\
 &= - \int_1^{\tau(\lambda, \mu)} (B(\lambda, T_s) - B(\lambda, T_p)) d\tau(\lambda, \mu, p)
 \end{aligned} \tag{2}$$

From the Planck function we find:

$$\Delta L = \frac{\partial B}{\partial T} \Delta T = \frac{\partial B}{\partial T} (T_s - T_\lambda) \tag{3}$$

For an optically thin gas the following approximations can be made:

$$d\tau = d\{\exp(-k_\lambda L)\} = k_\lambda dl \quad (4)$$

where k_λ is the absorption coefficient and l is the optical path-length. If we assume that the Planck function is adequately represented by a first order Taylor series expansion in each channel window, then:

$$B(\lambda, T_s) - B(\lambda, T_p) = \left. \frac{\partial B(\lambda, T_p)}{\partial T} \right|_{T_s} (T_p - T_s) \quad (5)$$

Substituting Equations 3, 4, 5 into Equation 2, we obtain:

$$T_s - T_\lambda = k_\lambda \int_1^\tau (T_s - T_p) dl \quad (6)$$

Therefore, if we pick two spectral regions of the atmosphere, we have two linear equations with different k_λ to solve simultaneously.

For example, if we consider the two channels as $\lambda=1$ and $\lambda=2$, then we obtain:

$$T_s - T_1 = -(T_s - T_2)k_1 / k_2 \quad (7)$$

or

$$T_s - T_1 = -(T_2 - T_1)k_1 / (k_2 - k_1) \quad (8)$$

Therefore the SST can be represented as:

$$T_s = c_0 + c_1 T_1 + c_2 T_2 \quad (9)$$

In general, this can be written as:

$$T_s = CT_b \quad (10)$$

The coefficient vector \mathbf{C} , which relates observed brightness temperatures to SST, is determined using regression methods by solving:

$$\mathbf{C} = \mathbf{YX}^T (\mathbf{XX}^T + k\mathbf{I})^{-1} \quad (11)$$

The \mathbf{Y} matrix contains a large number of training SSTs and the \mathbf{X} matrix contains brightness temperatures from VIIRS LWIR and MWIR channels. In general, the \mathbf{X} matrix may include nonlinear terms.

Figure 8 shows that the relationship between temperature deficits of AVHRR LWIR channel 4 and channel 5 is linear. The brightness temperatures from channel 4 are higher than those from channel 5. The differences between SST and brightness temperature are larger than 1 K and can be as large as 16 K.

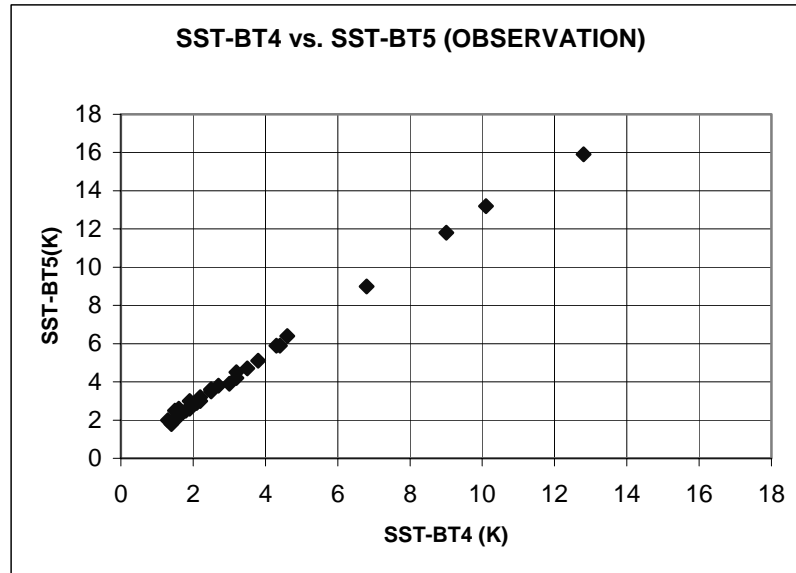


Figure 8. The relationship between temperature deficits at AVHRR channel 4 and channel 5 from observations.

Figure 9 is similar to Figure 8, but the data comes from the simulation of a transmittance model (Barton *et al.*, 1993). The maximum temperature deficit, approximately 10 K, is smaller than the observed deficits. The relationship is also linear. Compared to observed brightness temperatures, the model simulations showed a bias of 0.95 K at channel 4 and 1.36 K at channel 5.

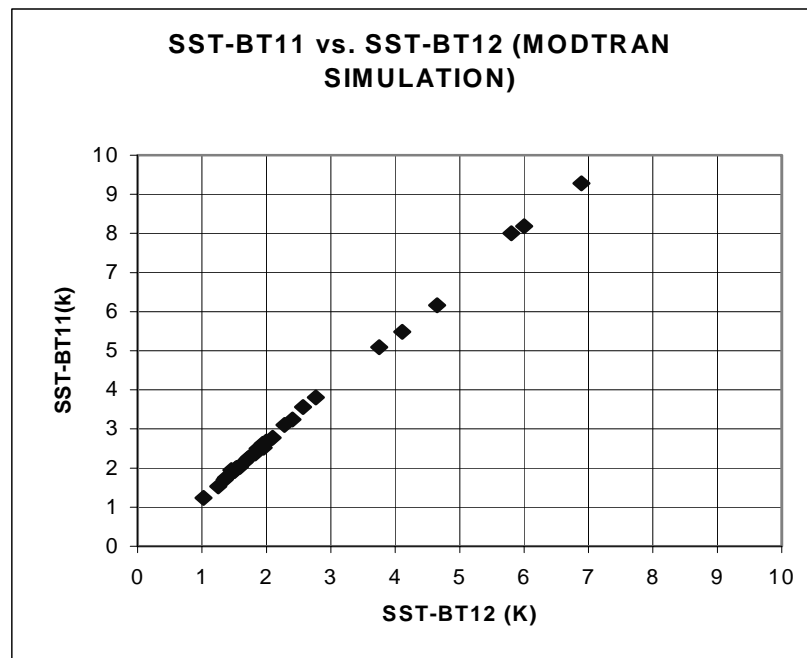


Figure 9. The relationship between temperature deficits at AVHRR channel 4 and channel 5 from simulation of a transmittance model

Figure 10 is similar to Figure 9, except that the data are obtained from MODTRAN simulations, and the maximum temperature deficit, approximately 10 K, is also smaller than observed deficits. The relationship is also linear. Compared to observed brightness temperatures, the MODTRAN simulations showed a bias of 0.51 K at channel 4 and 0.37 K at channel 5. The model error is much smaller in the MODTRAN simulation than that in Barton's transmittance model simulations. The large bias is caused by a few exceptional pixels. The temperature deficits of these pixels are larger than 10 K. By excluding these pixels and calibrating the simulation to observations, the differences can be reduced to < 0.1 K.

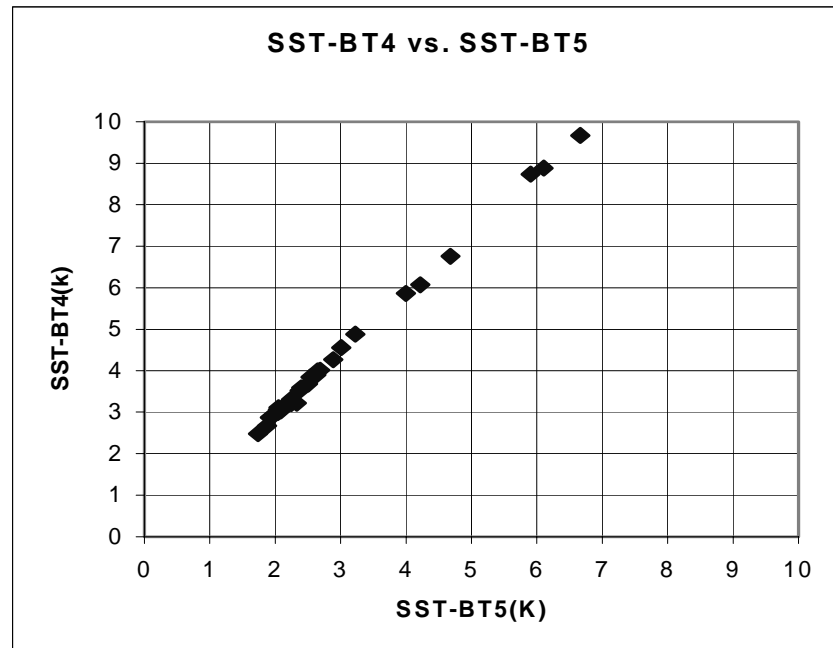


Figure 10. The relationship between temperature deficits at AVHRR channel 4 and channel 5 from MODTRAN simulations

These results suggest that the SST retrieval is basically a linear problem. Our testbed analyses of high-order nonlinear regression methods and neural network methods confirm that those methods do not provide significant improvements, and can deteriorate the results significantly for very noisy data. (For details, see Version 4 of this ATBD.)

If emissivity is treated as uniform for SST, Equation 1 can be solved numerically to retrieve T_s (SST) if the atmospheric profiles are known. However, it is very difficult and computationally consuming to solve Equation 1 unless we know exact atmospheric profiles. This is highly unlikely in the near future. Instead, highly accurate retrievals are performed on operational timescales using statistical regression methods.

3.3.2 Mathematical Description of the Algorithm

3.3.2.1 Regression Methods

The baseline VIIRS SST algorithm is based on statistical regression methods. Traditional statistical regression methods for satellite SST retrieval are linear or nonlinear MCSST. Because SST changes slowly with time, statistical methods has a great advantage to reach high accuracy if high quality *in situ* data are available. The ATSR-like physical retrieval is also a regression method. The difference between MCSST and ATSR SST is that the MCSST matches the TOA radiances with bulk SST, while ATSR SST retrieval is based on model simulations and retrieved skin SSTs. The following equations may be used for both MCSST, and ATSR-like skin SST retrieval. However the physics of the two methods are different.

Daytime algorithms:

Dual split window (10.8, 12, 3.7, 4.0 μm bands) algorithm: (new)

$$\begin{aligned} SST = & a_0 + a_1 T_{11} + a_2 T_{12} + a_3 (\sec(z) - 1) + a_4 T_{3.7} + a_5 T_{4.0} + a_6 T_{3.7} \cos(zs) \\ & + a_7 T_{4.0} \cos(zs) + a_8 (T_{11} - T_{12})^2 \end{aligned} \quad (12)$$

Split window (10.8 + 12 μm bands) nonlinear: (Modified from AVHRR operational, May *et al.*, 1998)

$$SST = a_0 + a_1 T_{11} + a_2 (T_{11} - T_{12}) + a_3 (\sec(z) - 1) + a_4 (T_{11} - T_{12})^2 \quad (13)$$

Nighttime algorithms:

Dual split window (10.8, 12, 3.7, 4.0 μm bands) algorithm: (new)

$$SST = a_0 + a_1 T_{11} + a_2 T_{12} + a_3 (\sec(z) - 1) + a_4 T_{3.7} + a_5 T_{4.0} + a_6 T_{3.7}^2 + a_7 T_{4.0}^2 + a_8 (T_{11} - T_{12})^2 \quad (14)$$

The VIIRS baseline algorithm uses equation 12 for daytime retrieval and equation 14 for nighttime retrieval (dual split window algorithm). Equation 13 (split window algorithm) is used as the VIIRS fallback algorithm during sun glint conditions. As discussed in version four of this ATBD, higher order polynomial terms and neural networks do not improve the results. Therefore, only second order polynomial terms are used in the VIIRS algorithm. In order to improve uncertainty and accuracy, the SST field is stratified into a few groups, and regression equations are derived for each group. It is necessary to continue validation studies to insure that the quadratic term is well-behaved in all conditions.

3.3.2.2 Enhancement of the dual split window algorithm

The VIIRS baseline algorithm is the dual split window algorithm using 10.8, 12, 3.7 and 4.0 μm , as defined in equation 12 for daytime, and equation 14 for nighttime. When MWIR

measurements are unavailable, such as solar glint conditions, the split window algorithm (equation 13) are used as the fallback algorithm. Figure 11 shows a sun glint case in the TRMM observation. TRMM VIRS 3.7 μm and visible 0.66 μm band radiances significantly increase in solar glint area. The sun glint has negligible effect on LWIR measurements.

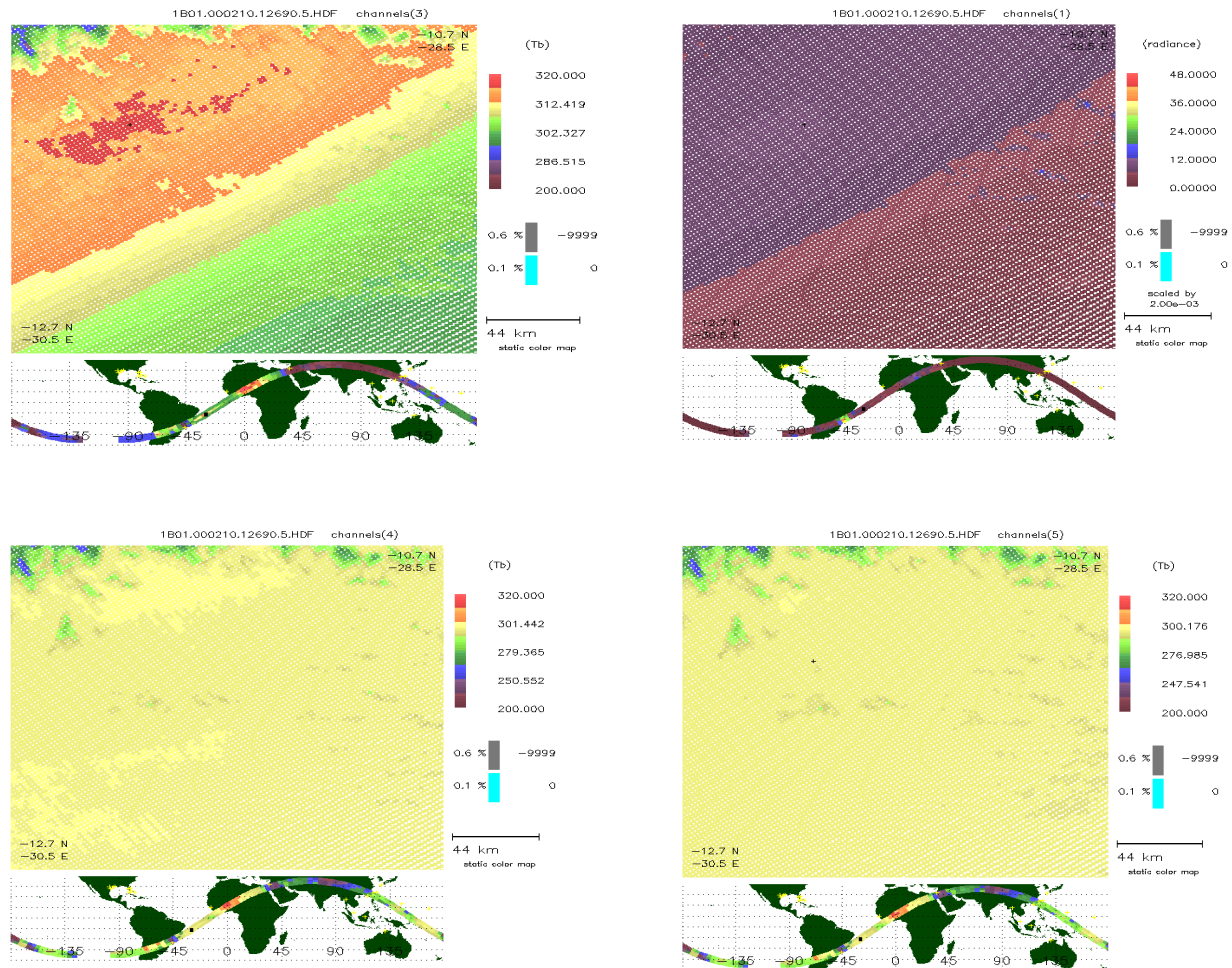


Figure 11. TRMM VIRS channel 3 brightness temperature (3.7 μm), channel 1 (0.66 μm) reflectance, Channel 4 (11 μm) brightness temperature, and channel 5 (12 μm) brightness temperature.

Performance of the baseline algorithm is enhanced by separating the algorithm into two categories at a threshold 10.8 μm brightness temperature of 282 K. Therefore, in the baseline algorithm, there are a total of 2 sets of regression coefficients in both daytime and nighttime. In this way, the dual split window algorithm works well at both warm and cold temperatures. 10.8 μm brightness temperature plays the major role at colder temperatures, while 4.0 μm brightness temperature plays the major role at warmer temperatures.

Analysis of the global SST retrieval error has demonstrated that larger errors are associated with air mass attributes. In order to reduce the error, an air mass classification technique was introduced into the VIIRS SST retrieval. Figure 12 and Figure 13 shows the flow process of this method. In this method, Precipitable Water (PW) is used as a decision tool for classification, but

not as a parameter in the SST equation, such that the error in PW will not contribute significantly to the SST retrieval.

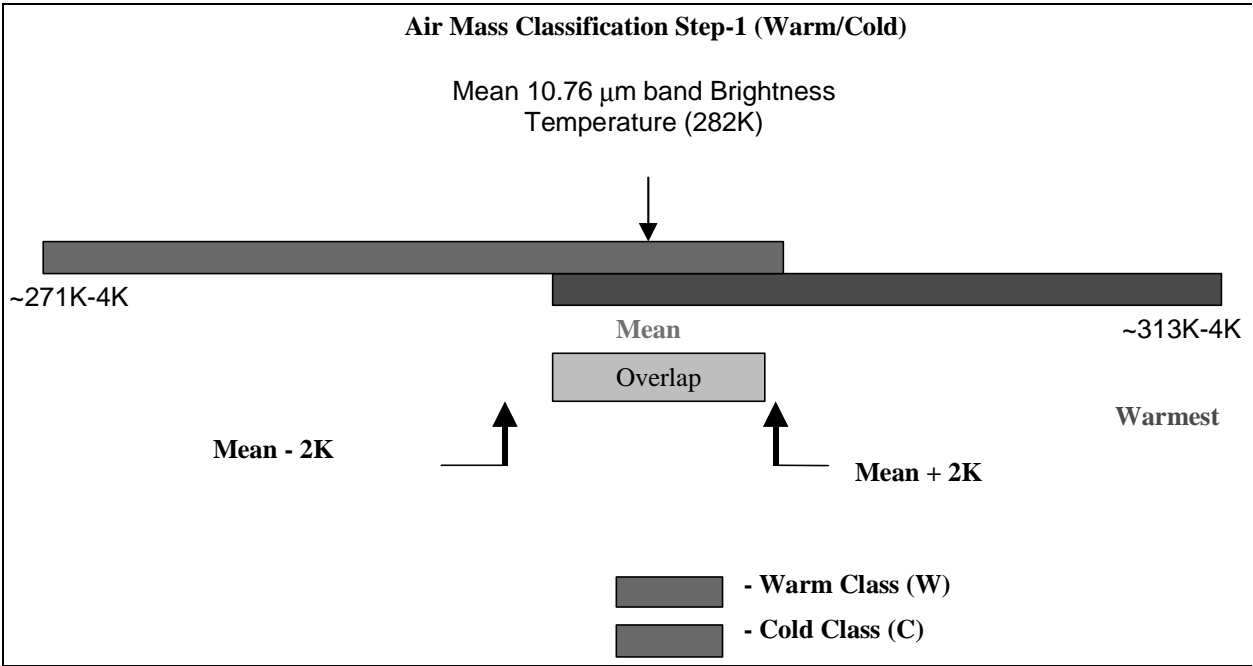


Figure 12. Air mass classification diagram – step 1 (warm/cold)

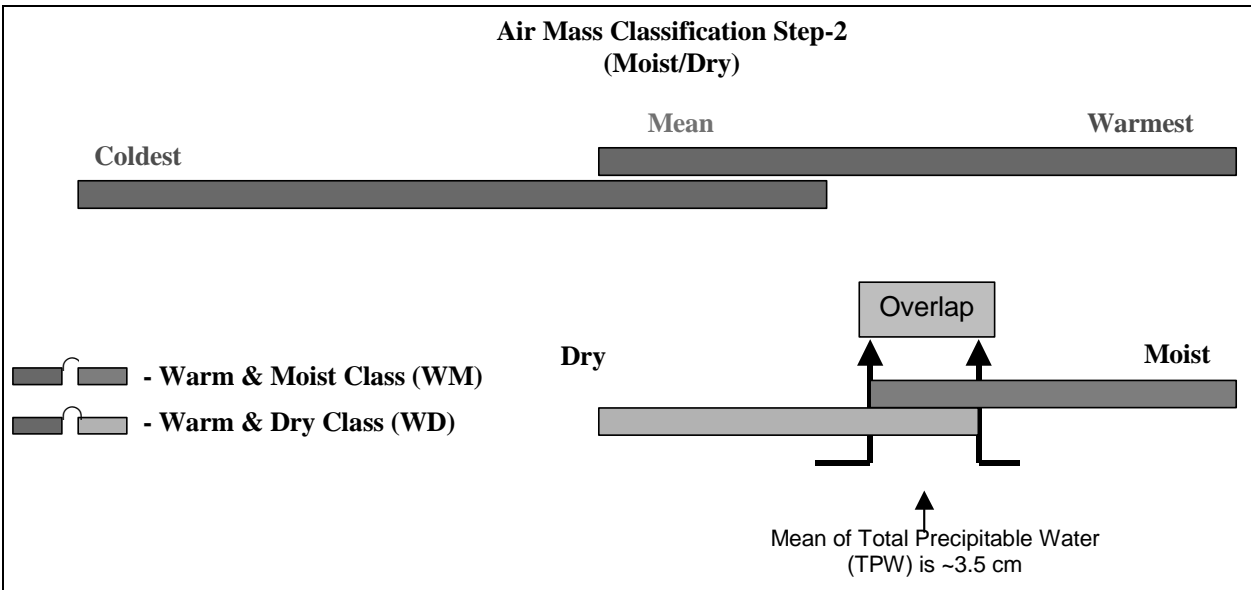


Figure 13. Air mass classification diagram –step 2 (moist/dry).

Figure 14 shows the improvement in the SST retrieval error due to the air mass classification enhancements added to the VIIRS baseline dual split window algorithm. With the air mass classification method, the maximum error is reduced to 0.8 K from 1.67 K. The maximum errors along the California coast and South Africa coast are reduced significantly. The precision for the baseline algorithm with daytime and nighttime classification is 0.21 K before enhancement. It is improved to 0.17 K using an additional warm and cold classification, and to 0.17 K if moist and dry classification is added..

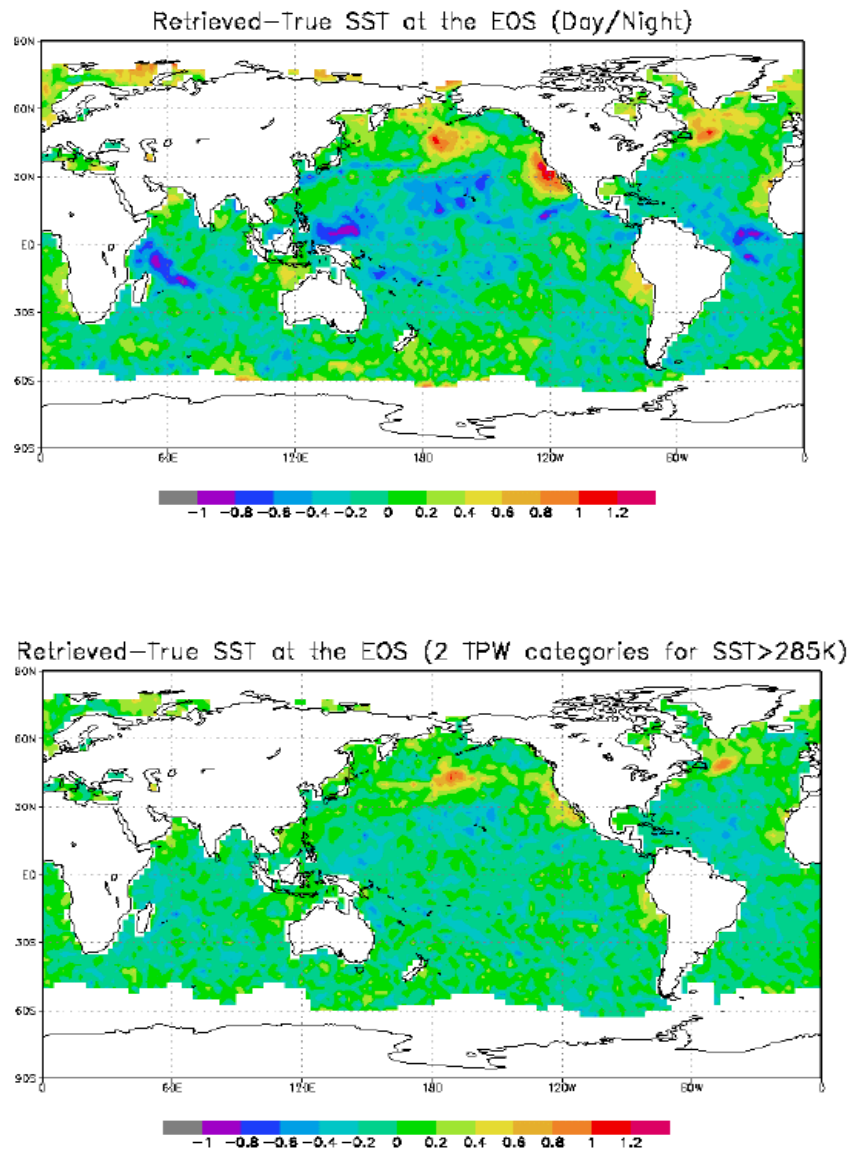


Figure 14. SST bias comparison between unimproved VIIRS baseline dual split window algorithm and the algorithm with air mass classification enhancements.

3.3.3 Algorithm Output

SST is retrieved at pixel level for all satellite viewing angles, for all pixels that are not flagged as confident cloudy by the VIIRS cloud mask. Four VIIRS MWIR and LWIR bands are used in the VIIRS baseline dual split window algorithm, except in sun glint conditions, when two VIIRS LWIR bands are used in the VIIRS fallback split window algorithm. Separate sets of algorithm coefficients are used for bulk SST or skin SST; for day without sunglint, day with sunglint, or night; for warm moist conditions, warm dry conditions, or cold conditions.

3.3.4 Variance and Uncertainty Estimate

The SST retrieval uncertainty is defined as the square root of the sum of accuracy squared plus precision squared. SST uncertainties are approximately 0.3 K for the VIIRS baseline dual split window algorithm and 0.5 K for the VIIRS fallback split window algorithm.

Figure 15 shows the specified and predicted uncertainty for the VIIRS baseline dual split window algorithm with all error sources accounted for, using the 305-profile data set with daytime simulation. The solar zenith angle is between 10 to 60 degree. Viewing angle is between 0 to 45 degree.

Figure 15 shows that there is no significant difference between specified sensor noise and predicted sensor noise. Under most conditions, the VIIRS baseline dual split window algorithm achieves 0.29 K precision CAIV target and 0.35 K uncertainty objective.

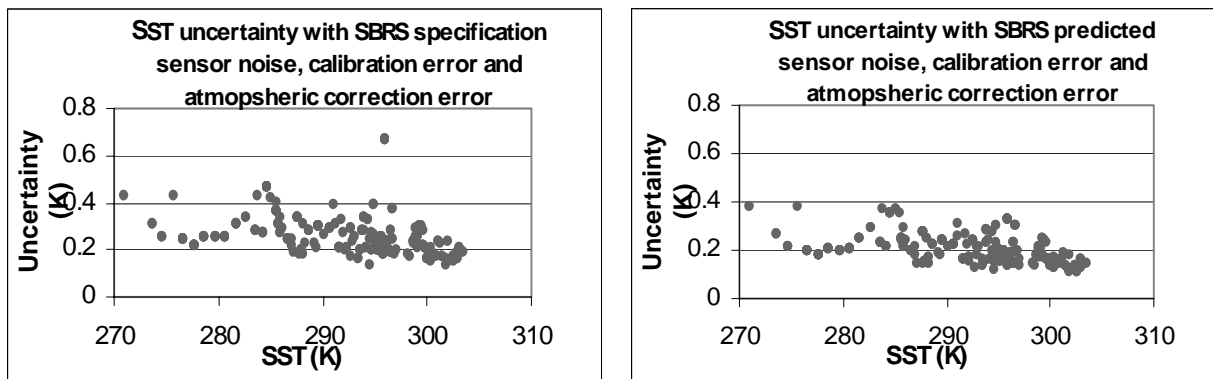


Figure 15. The total uncertainty with all error sources including SBRS calibration perturbation, specified and predicted sensor noises, for the VIIRS baseline dual split window algorithm. (a) Uncertainty from the specified sensor noise, (b) Uncertainty from the predicted sensor noise.

3.4 ALGORITHM SENSITIVITY STUDIES

3.4.1 Test Data Sets

We used three data sets to estimate the SST retrieval uncertainty

- The first is a data set of 299 global observations of skin SST with radiosonde atmospheric profiles and coincident satellite passes (Emery *et al.*, 1994) plus 6 standard atmosphere profiles and surface temperatures. In order to simulate the daytime radiance, 400 simulations were performed for each pixel, in order to employ different satellite viewing angles, solar zenith angles and azimuth angles. There are 121,170 samples. The samples for seven SST categories from 270-275 K to 300-305 K are 240; 1,160; 1,120; 2,200; 2,120; 3,917; and 1,360. Half of the data were randomly picked as training data, others as testing data. Sensor noises are applied to both training and testing data. Absolute radiometric errors (0.4%) were applied only to testing data.
- The second data set is a global NCEP snapshot of surface temperature at 2.5° x 2.5° resolution supplied by NCEP (Kalnay *et al.*, 1996), with matching atmospheric profiles. There are 26,590 samples in the simulation. The samples for seven SST categories from 270-275 K to 300-305 K are 100, 343, 405, 310, 318, 910, and 265.
- The third data set is a 1.3 km resolution surface temperature scene derived from AVHRR 1b data.

In Figure 16, panel (a) shows the range of 299 SSTs. Simulations were performed for nighttime and daytime. The NEdT values are 0.08 K for the 10.8 μm band, 0.1 K for the 12 μm band, and 0.15 K for the 3.7 μm band. The differences between observed and retrieved SSTs for the VIIRS fallback split window retrieval are shown in panel b. Calibration errors were not considered in this example.

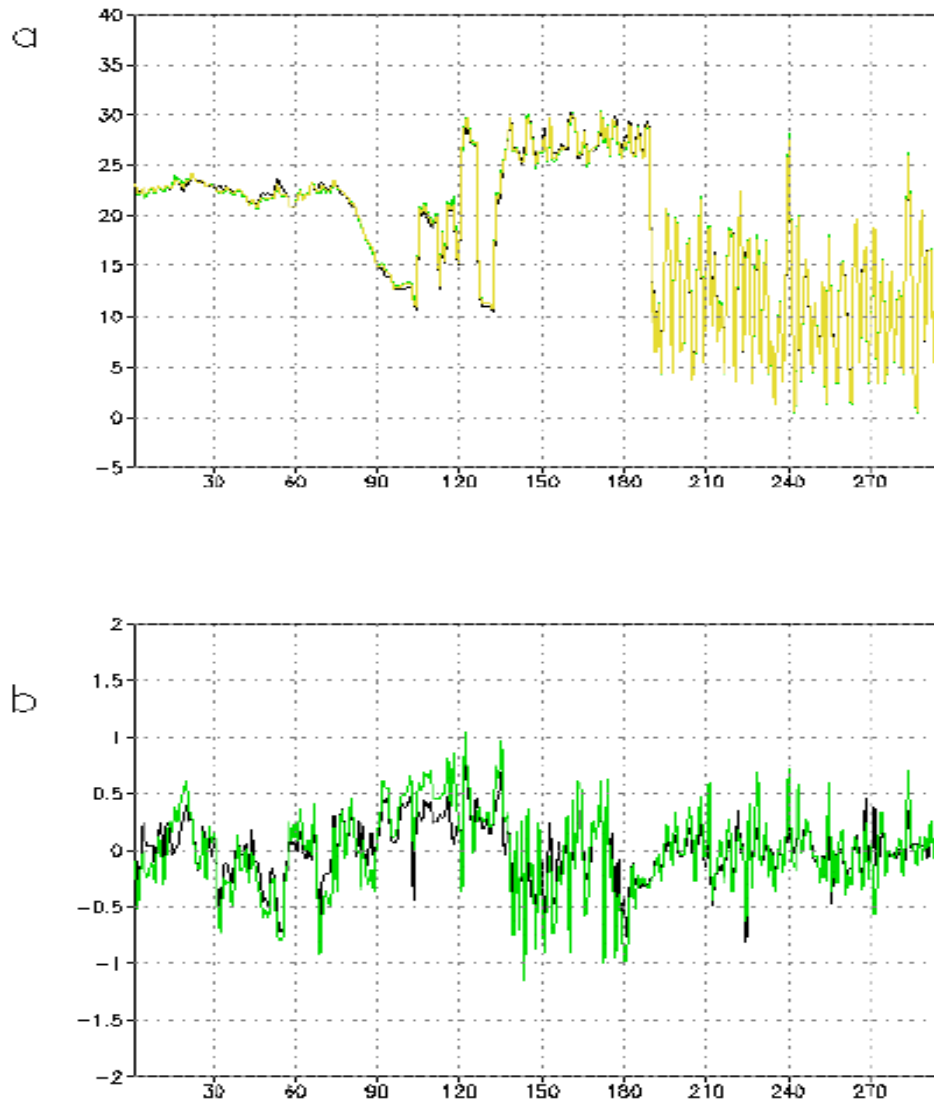


Figure 16. (a) Range of the 299 ship-observed SSTs. (b) Difference between true SST and retrieved SST. Green line: daytime. Black line: nighttime.

In Figure 17, panel (a) shows the global NCEP snapshot SST field at 00Z July 1, 1993 and panel (b) shows the SST retrieved from MODTRAN simulations. Panel (c) is the difference between retrieved and observed SSTs. The Root Mean Squared (RMS) error is 0.45 K at the 0.1 K instrument noise level.

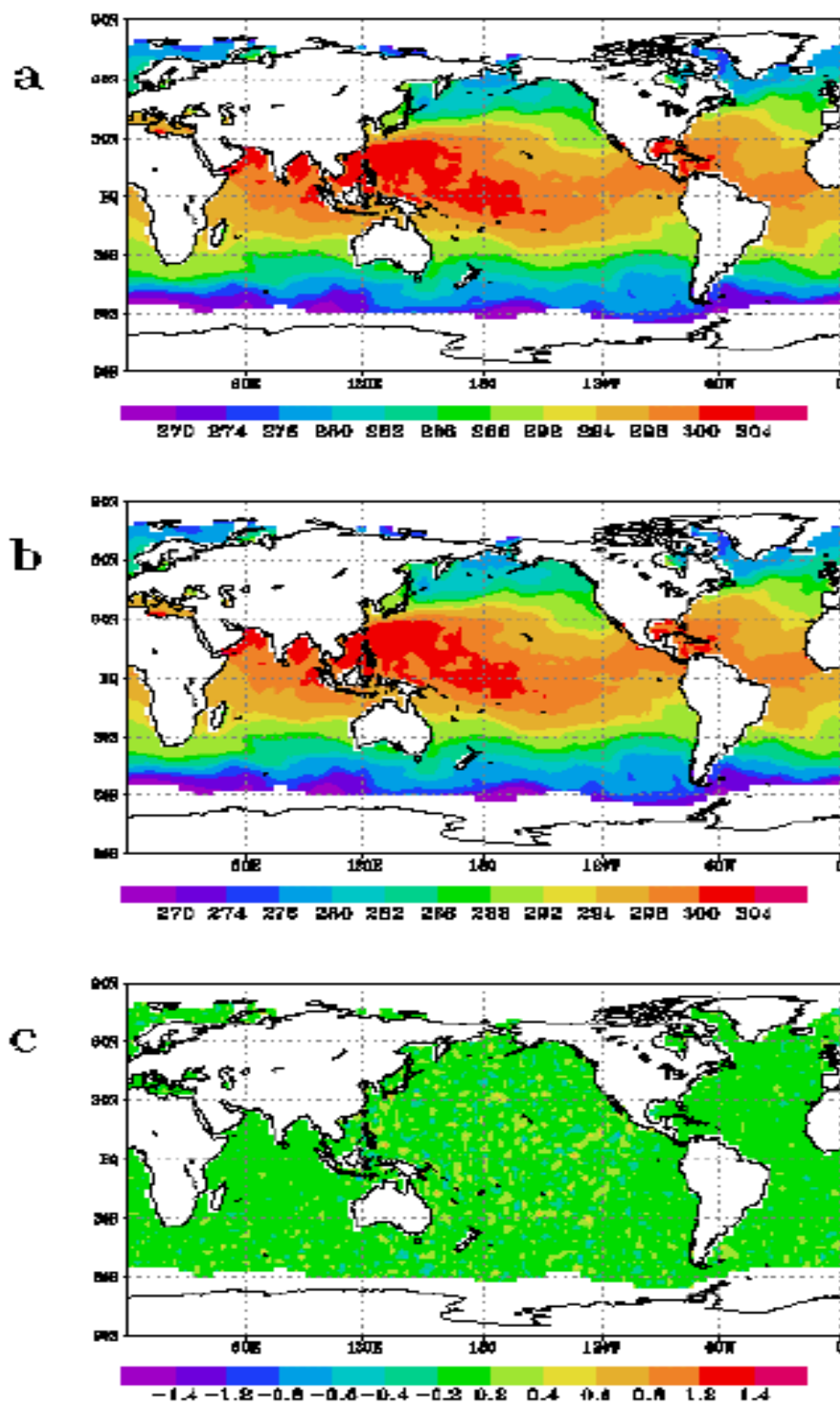


Figure 17. a. Global SST. b. Retrieved SST. c. The difference between global and retrieved SSTs

In Figure 18, panel (a) is a 1 km resolution SST scene off the Florida coast which is derived from AVHRR 1B data. Two methods were used to retrieve SSTs. One uses 25% of the data as training data to retrieve the SST. The RMS error is 0.3 K for the VIIRS baseline dual split window algorithm. Because this simulation only included nine atmospheric profiles, the atmospheric correction error is underestimated. The other uses equations derived from the global NCEP snapshot SST to retrieve the high resolution SST. The uncertainty is 0.45 K for the VIIRS fallback split window.

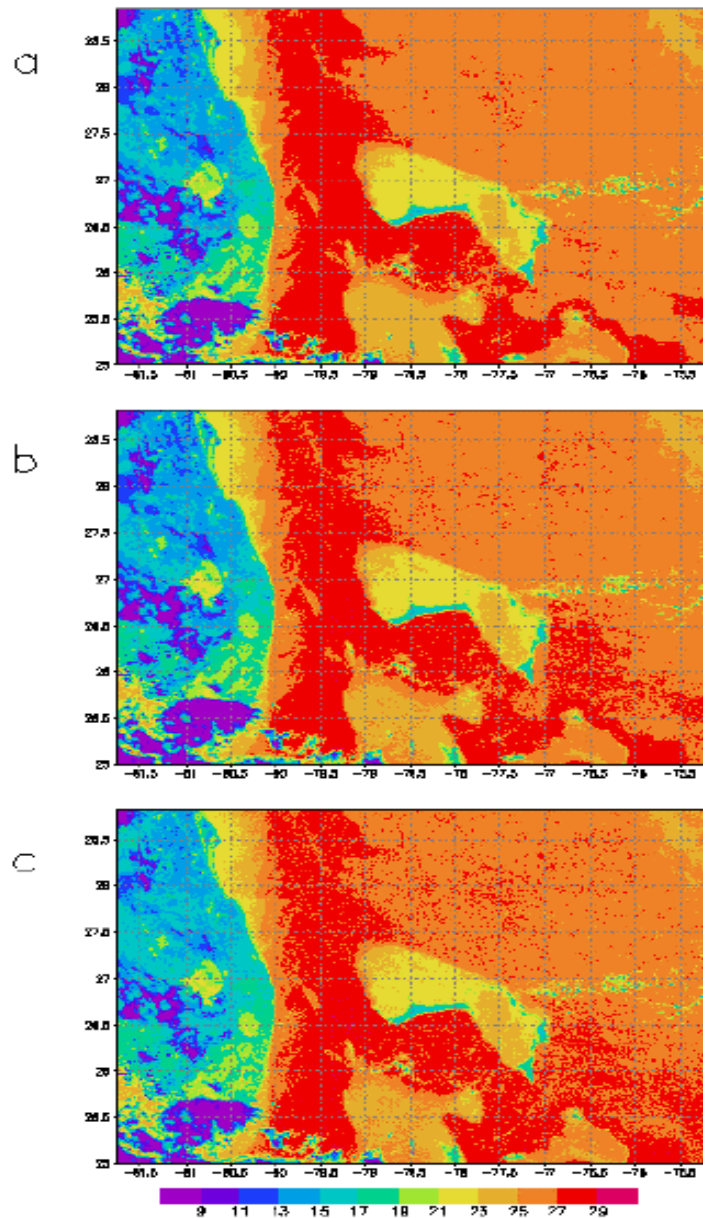


Figure 18. a. Observed 1 km SST. b. Retrieved SST using equation derived from 25% of the observed data. c. Retrieved SST using equation derived from global NCEP data. The noise was added by using the SBRS sensor noise model 3.

3.4.2 Sensor Noise Effects

The sources of error in accuracy and precision are:

- Atmospheric correction
- NedT
- Calibration
- BBR
- MTF

The VIIRS baseline dual split window algorithm provides excellent atmospheric correction. The sensor noise is not amplified by the algorithm. Table 3 shows the comparison of contributions to errors from sensor noise and atmospheric corrections, using rigorous single-pixel NEdT noise models. The noise models are a set of parameterized sensor noise levels simulated by SBRS' radiometric model. Model 1 was best, model 7 was worst, and model 3 was closest to the sensor specification for NEdT.

Table 3. Comparisons of the dual split window SST Precision

Noise Model	NEdT (K)				Sensor Contribution to precision (K)	Atmosphere correction to precision (K)	Total Precision (K)
	3.7 •m band	4.0 •m band	10.8 •m band	12 •m band			
Noise Free	0.	0.	0.	0.	0.	0.18	0.18
Model 1	0.12	0.10	0.04	0.05	0.11	0.18	0.21
Model 2	0.14	0.12	0.06	0.07	0.15	0.18	0.23
Model 3	0.18	0.15	0.08	0.10	0.18	0.18	0.25

The atmosphere is transparent in the MWIR bands and present an effective correction for water vapor. Because the MWIR bands are contaminated by the solar radiation, the MWIR bands were historically used to retrieve SST only at night. The VIIRS baseline dual split window algorithm is effective because a solar radiation correction was implemented in the MWIR window.

The global data set includes atmospheric profiles and surface temperatures. This data set has 17 levels of the atmosphere and the fields are smoothed. Using this data set, the precision of the VIIRS baseline dual split window algorithm is usually less than 0.3 K for sensor noise model 3. Figure 19 shows the daytime and nighttime precision as a function of satellite viewing angles and temperature values for the VIIRS baseline dual split window algorithm. The VIIRS baseline dual split window algorithm (3.7, 4.0, 10.8 and 12.0 μm) meets the threshold requirement at anytime, and over any range for sensor model 3.

Global Daytime 4-band SST PRECISION Global Nighttime 4-band SST PRECISION

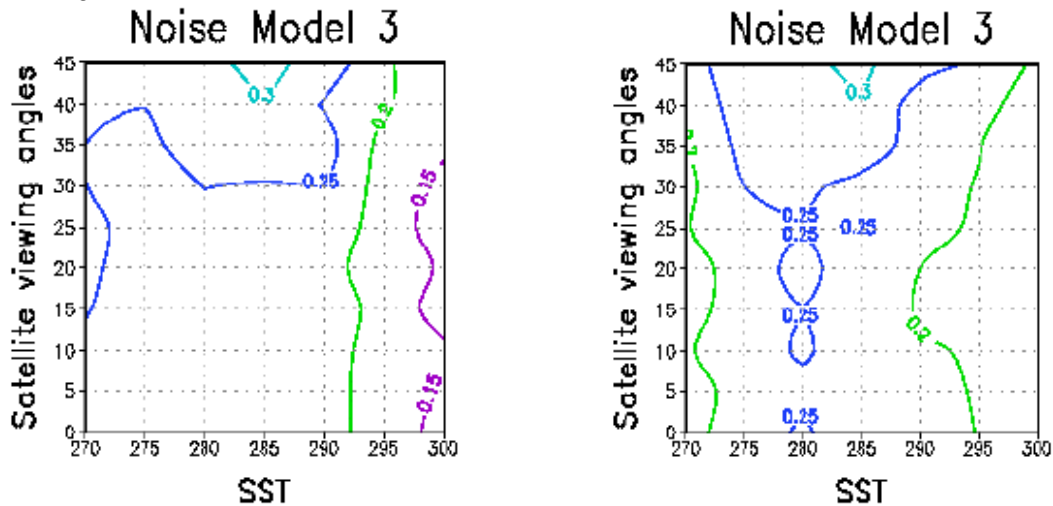


Figure 19. Dual split window (3.7, 4.0, 10.8, 12.0 μm) SST precision as function of satellite viewing angle and SST range. (a) Daytime. (b) Nighttime

3.4.3 Water Vapor Effects

Figure 20 and Figure 21 show the SST retrieved error including precision, accuracy and uncertainty for the VIIRS baseline dual split window algorithm and VIIRS fallback split window algorithm. The dual split window algorithm meets the threshold for all total column water vapor ranges. For the split window, SST precision is greater than the threshold 0.45 K if total column water vapor above 4.2 cm.

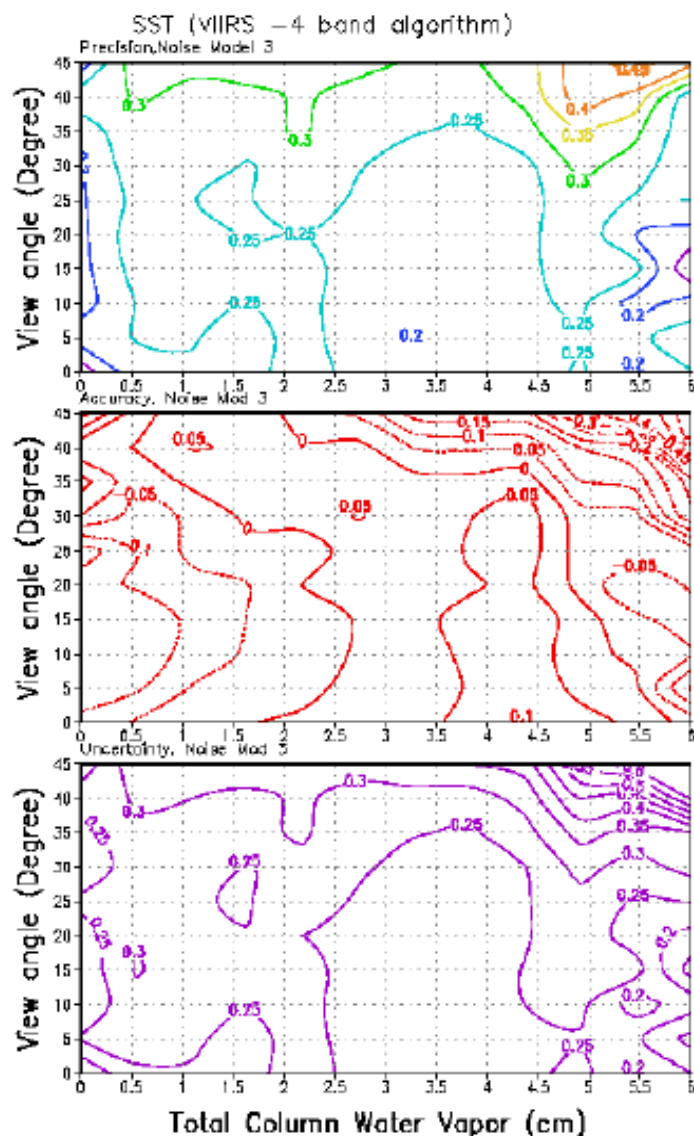


Figure 20. The SST retrieval error distribution vs. sensor viewing angle and total column water vapor for sensor noise model 3 for the VIIRS baseline dual split window algorithm. Upper Panel (Precision), Middle (Accuracy), Bottom (uncertainty)

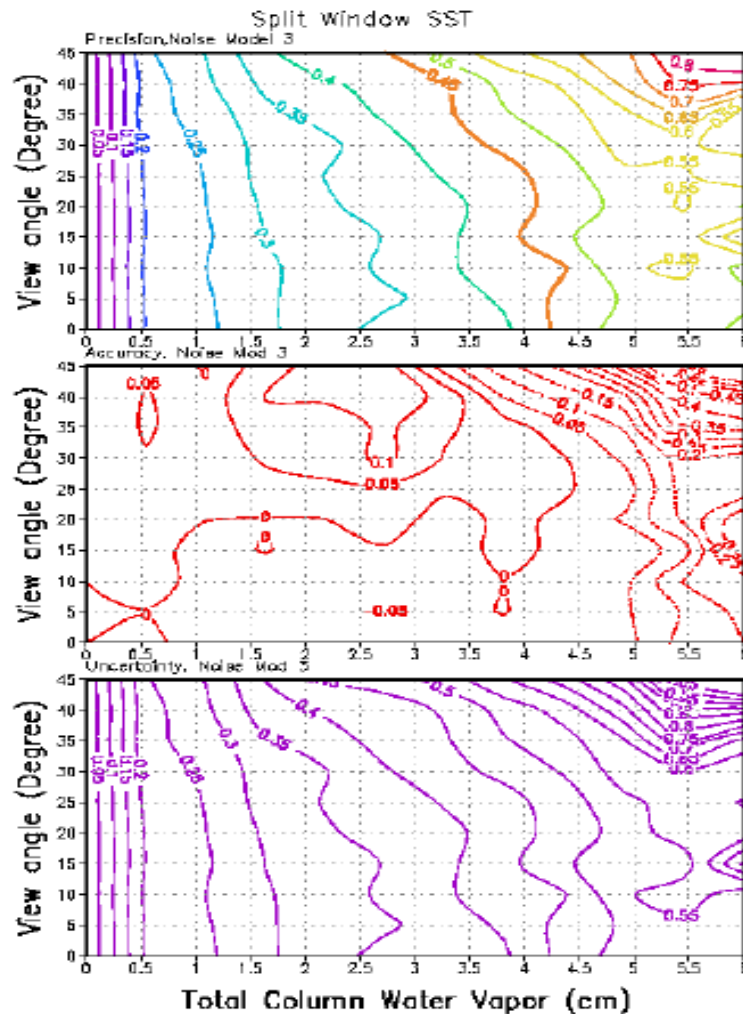


Figure 21. The SST retrieval error distribution vs. sensor viewing angle and total column water vapor for sensor noise model 3 for the VIIRS fallback split window algorithm. Upper Panel (Precision), Middle (Accuracy), Bottom (uncertainty)

3.4.4 Calibration Errors

In order to investigate the algorithm accuracy requirement relevant to the mean radiometric error in the sensor, we added mean errors to the simulated radiances and performed the VIIRS baseline dual split window algorithm and the VIIRS fallback split window algorithm. There were 299 skin SST and atmospheric profiles used in this simulation.

Figure 22 shows the dual split window accuracy change with the mean error added to the radiance for each band. The data is from global observations. In order to meet the 0.2 K accuracy, the uncorrelated calibration error needs to be less than 0.2%. However, if the error in the four bands are correlated, the calibration requirement may be relaxed to 0.4%. Figure 23 is similar to Figure 22, but for the split window algorithm. In order to meet the 0.2 K accuracy, the uncorrelated calibration error needs to be less than 0.15%. If the error in the two LWIR bands are correlated, the calibration requirement may be relaxed to 0.4%.

4-band SST Accuracy v.s. Calibration errors

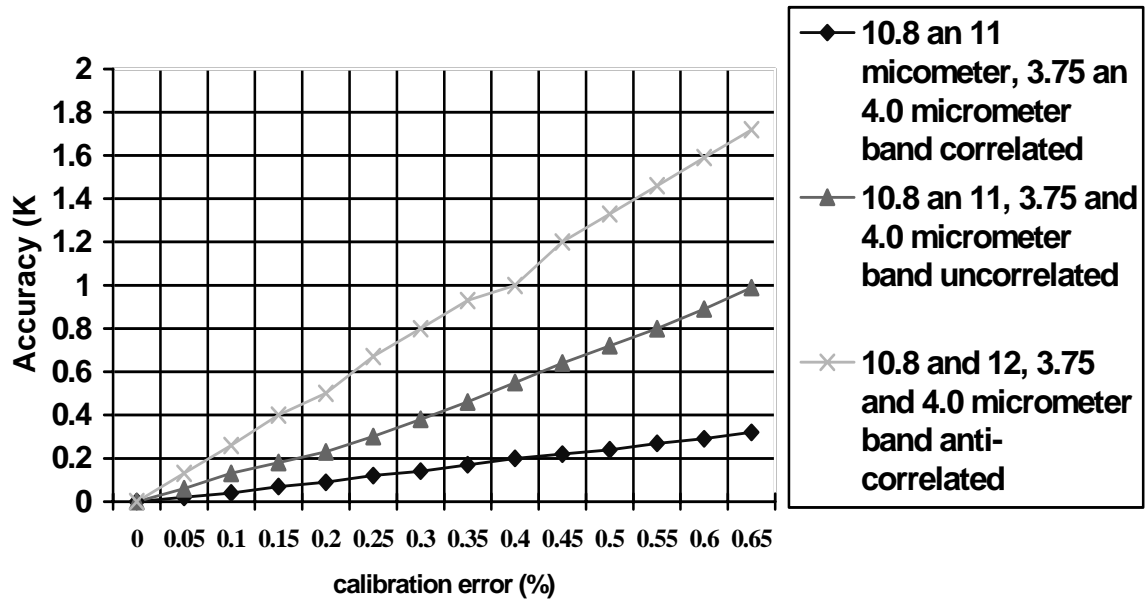


Figure 22. Dual split window SST accuracy relevant to calibration error.

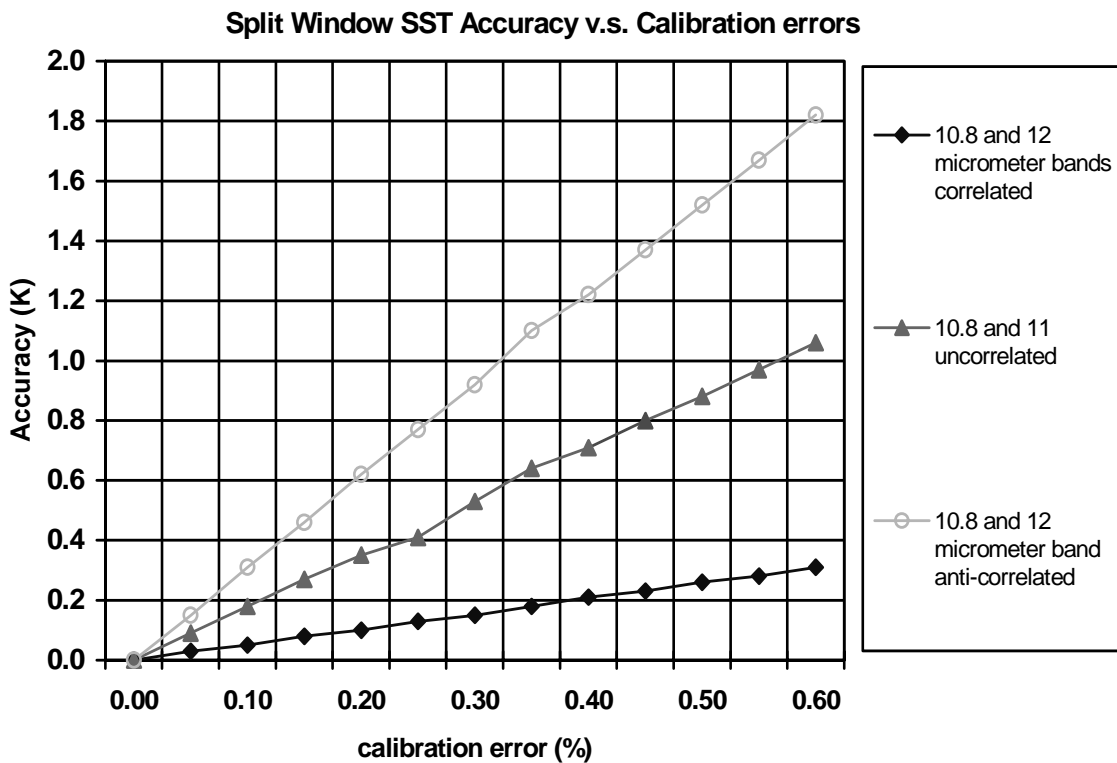


Figure 23. Split window SST accuracy relevant to calibration error.

Table 4 shows the fractional VIIRS radiance uncertainty and Table 5 shows the converted scene temperature uncertainty.

Table 4. VIIRS Fractional Radiance Uncertainty

Temp (K)	VIIRS Bands (μm)			
	3.7	4.0	10.8	12
260	.0083	.0071	.0031	.0031
270	.0079	.0067	.0031	.0031
280	.0074	.0064	.0031	.0031
290	.007	.0061	.0031	.0031
300	.0067	.0058	.003	.0031
310	.0064	.0055	.003	.003
320	.0061	.0053	.003	.003

Table 5. Scene Temperature Uncertainty

Temp (K)	VIIRS Bands (μm)			
	3.7	4.0	10.8	12
260	0.15	0.13	0.16	0.18
270	0.15	0.14	0.17	0.19
280	0.15	0.14	0.18	0.2
290	0.15	0.14	0.19	0.21
300	0.16	0.14	0.2	0.22
310	0.16	0.15	0.22	0.24
320	0.16	0.15	0.23	0.25

The analysis of uncertainty for the 10.8 μm band ($\rho_{\text{ev}}=0.01$) is shown in Figure 24. It indicates various error sources that contribute to the uncertainty of the VIIRS radiances, such as the variability of Response Versus Scan angle (RVS), the band center, the black body temperature, etc. Figure 25 shows the variation of ρ_{ev} as a function of Angle Of Incidence (AOI) for the 10.8 μm band. The data set used in this test is NCEP global data set. One quarter of the data were used as training data, and the rest as testing data. The radiometric errors were added only to the test data. The viewing angles vary from -45° to 45° , corresponding to AOI from 25° to 65° .

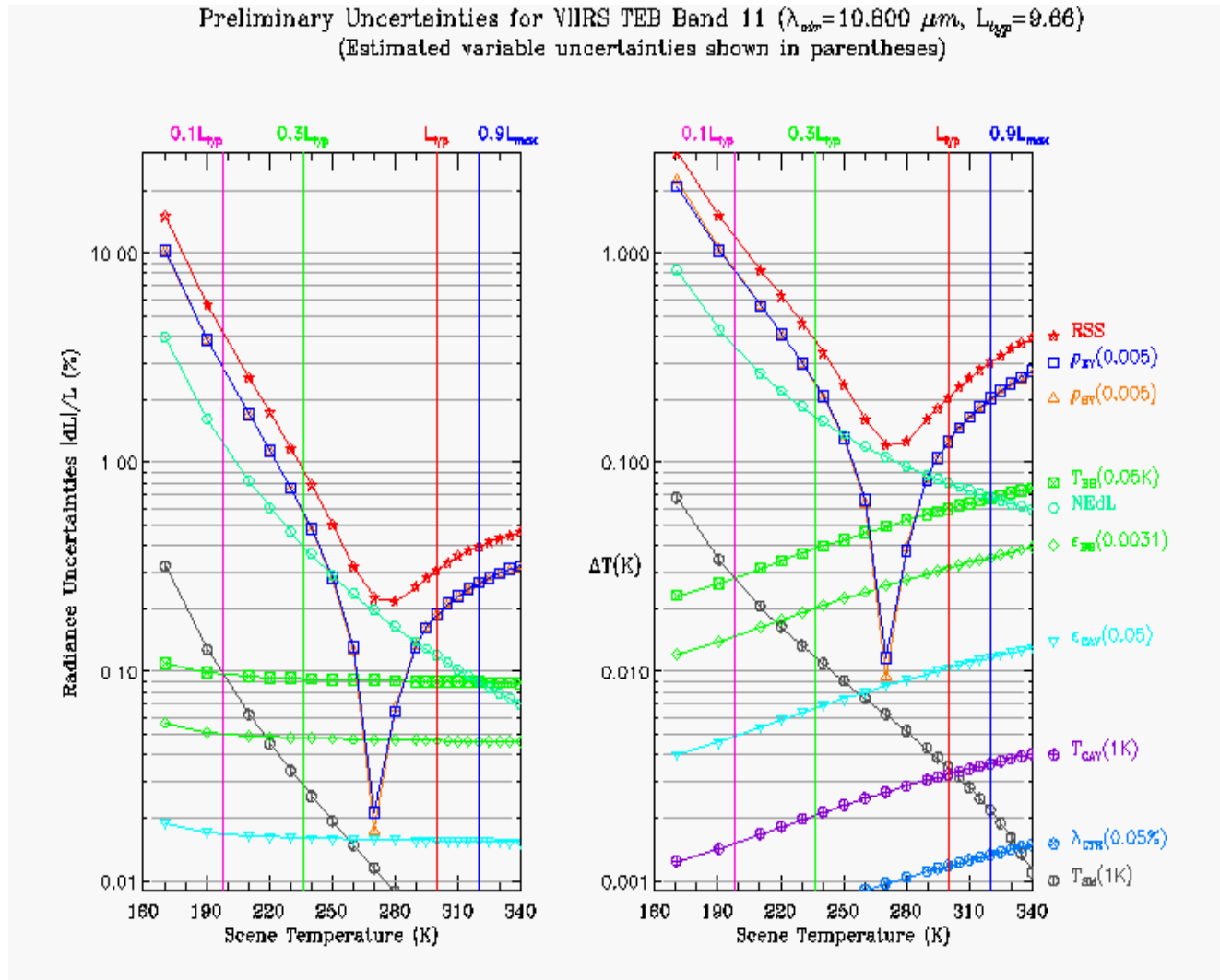


Figure 24. Uncertainties for the VIIRS 10.8 μm band.

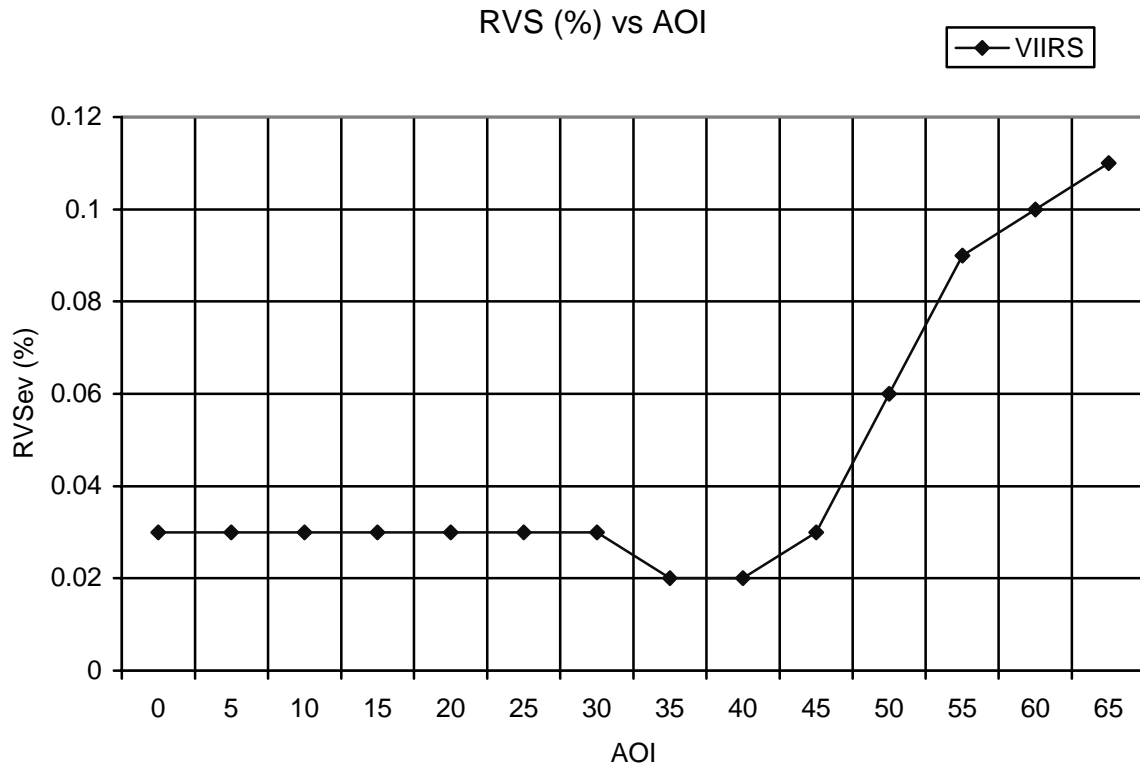


Figure 25. ρ_{ev} as a function of satellite viewing angle for the VIIRS 10.8 μm band.

Results From Radiosonde Data

In order to test calibration models, we used random calibration perturbation for 305 radiosonde profiles with solar zenith angle changes from 10 to 60 degree (daytime) and viewing zenith angle changes from 0 to 45 degree. There are a total of 15250 calibration perturbations.

Figure 26 shows the results of the daytime VIIRS baseline dual split window solution, assuming the radiometric errors for all bands are positively correlated. The upper panel is the SST accuracy due to the algorithm only. The middle panel shows the total accuracy error. For global data, the mean error is small. The accuracy is dominated by the sensor error. The lower panel is the sensor contribution. In this case, the sensor contribution to the SST accuracy averages 0.14-0.17 K. The requirement is met for almost all SST ranges. The sensor contribution does not vary with satellite viewing angle since there is no AOI dependent information in this data.

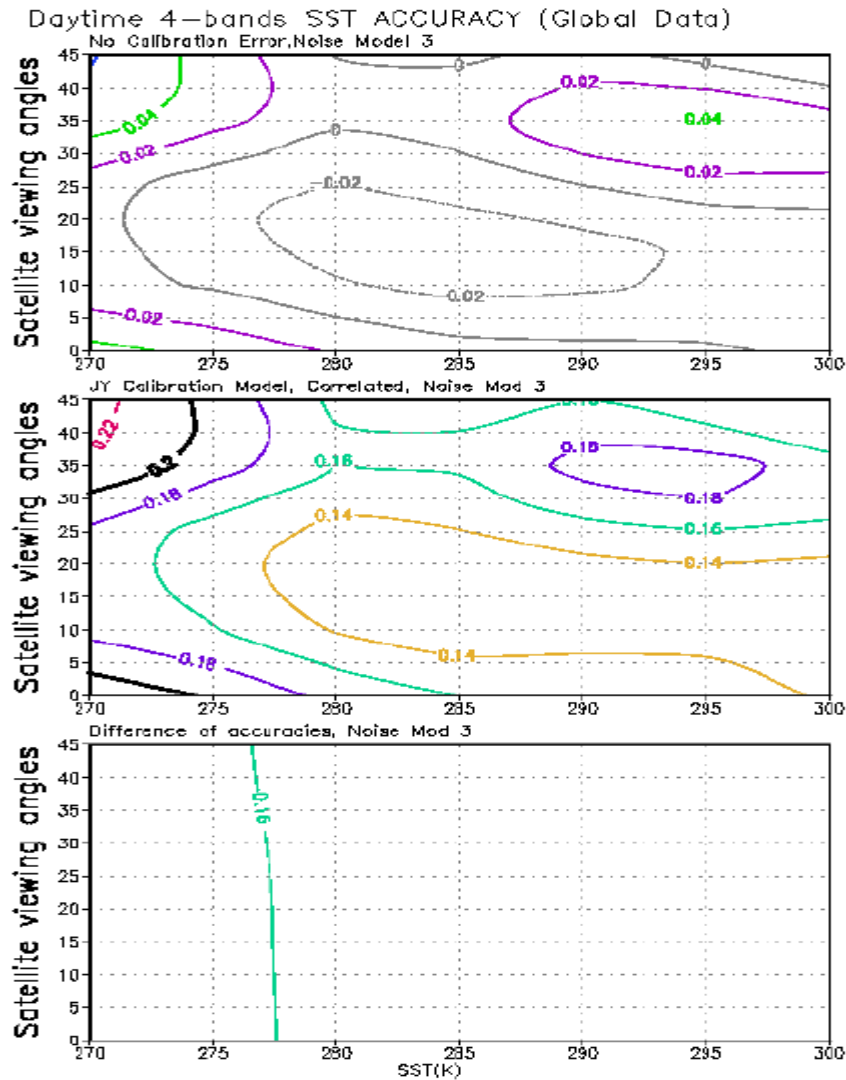


Figure 26. VIIRS baseline dual split window SST accuracy derived from NCEP data, assuming errors for all bands are correlated

Figure 27 shows the VIIRS baseline dual split window daytime SST accuracy, assuming the errors for all bands are not correlated. It indicates that the sensor failed to meet the 0.2 K accuracy requirement for the colder SST fields for non-correlated errors.

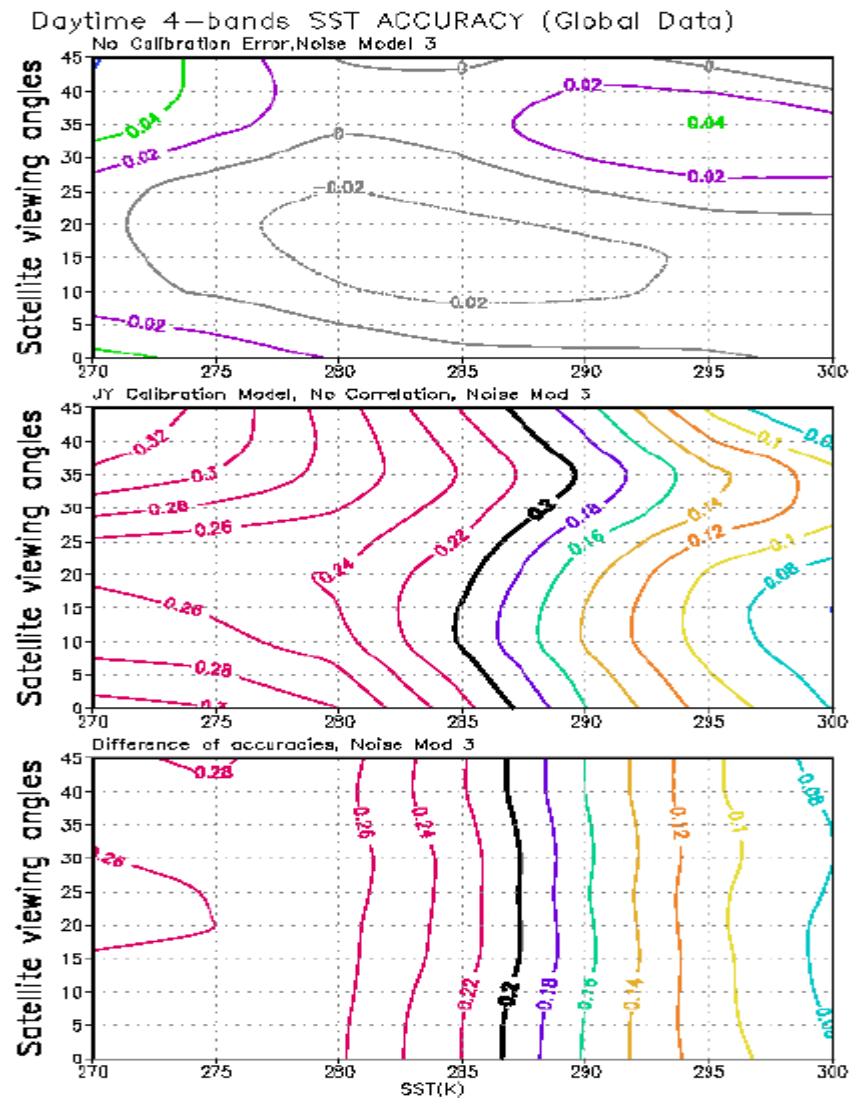


Figure 27. VIIRS baseline dual split window SST accuracy derived from NCEP data, assuming errors for all bands are not correlated.

Figure 28 shows the results of the daytime VIIRS fallback split window solution, assuming the radiometric error for all bands are positively correlated. In this case, the sensor contribution is < 0.17 K. However, the overall errors over some particular areas are larger than 0.2 K.

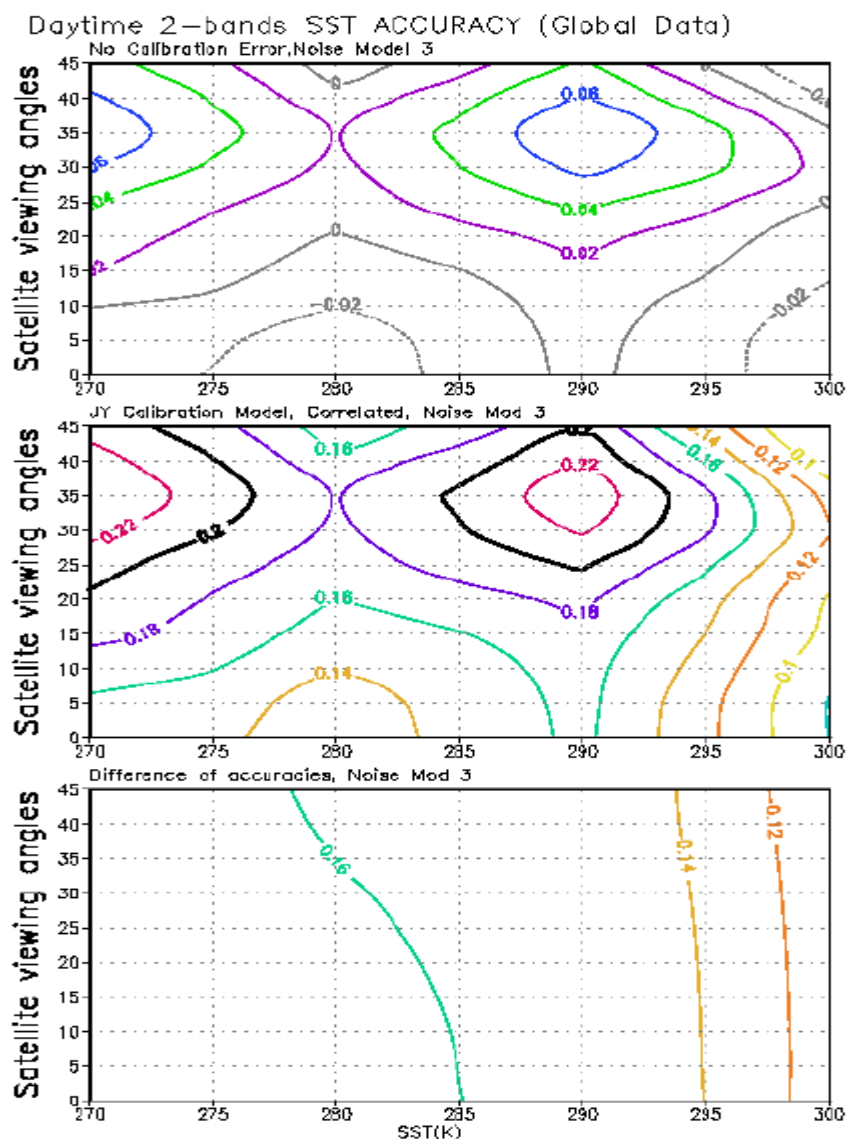


Figure 28. VIIRS fallback split window SST accuracy derived from NCEP data, assuming errors for all bands are correlated.

Figure 29 shows the VIIRS fallback split window daytime SST accuracy, assuming the errors for all bands are not correlated. It indicates that the sensor failed to meet the 0.2 K accuracy requirement for all SST ranges for non-correlated errors.

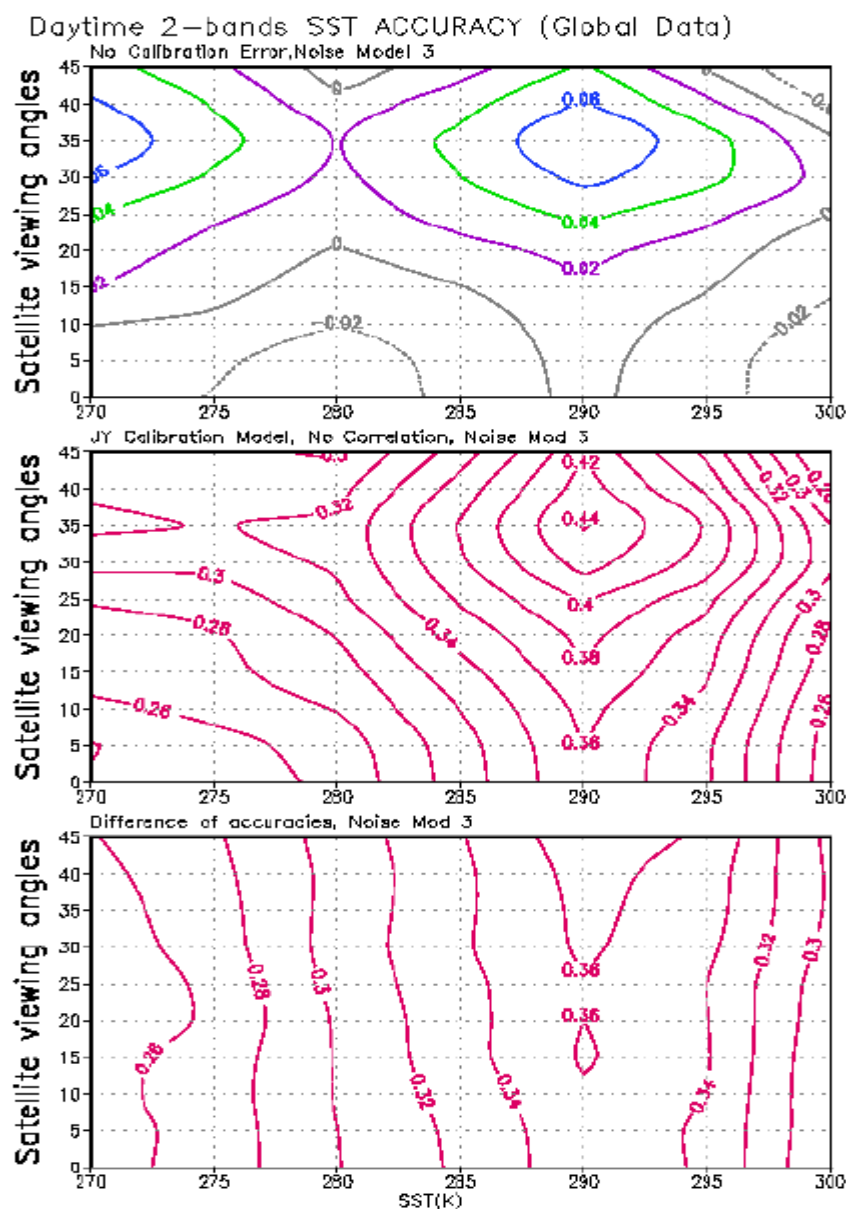


Figure 29. VIIRS fallback split window SST accuracy derived from NCEP data, assuming errors for all bands are not correlated.

Figure 30 shows the SST retrieval RMS accuracy from SBRS 192 calibration perturbation models to the five typical SST at the six different standard atmospheric conditions in MODTRAN (tropical, midlatitude summer and winter, subarctic summer and winter, and US standard). Because the retrieved SST bias from random calibration perturbation models may cancel each other, the absolute bias are taken to be averaged as RMS accuracy. The accuracy of the VIIRS baseline algorithm is less than 0.2 K at all temperatures, even though the error is higher at temperatures above 285 K. At warmer temperatures, the accuracy of split window algorithm is greater than our specification 0.2 K.

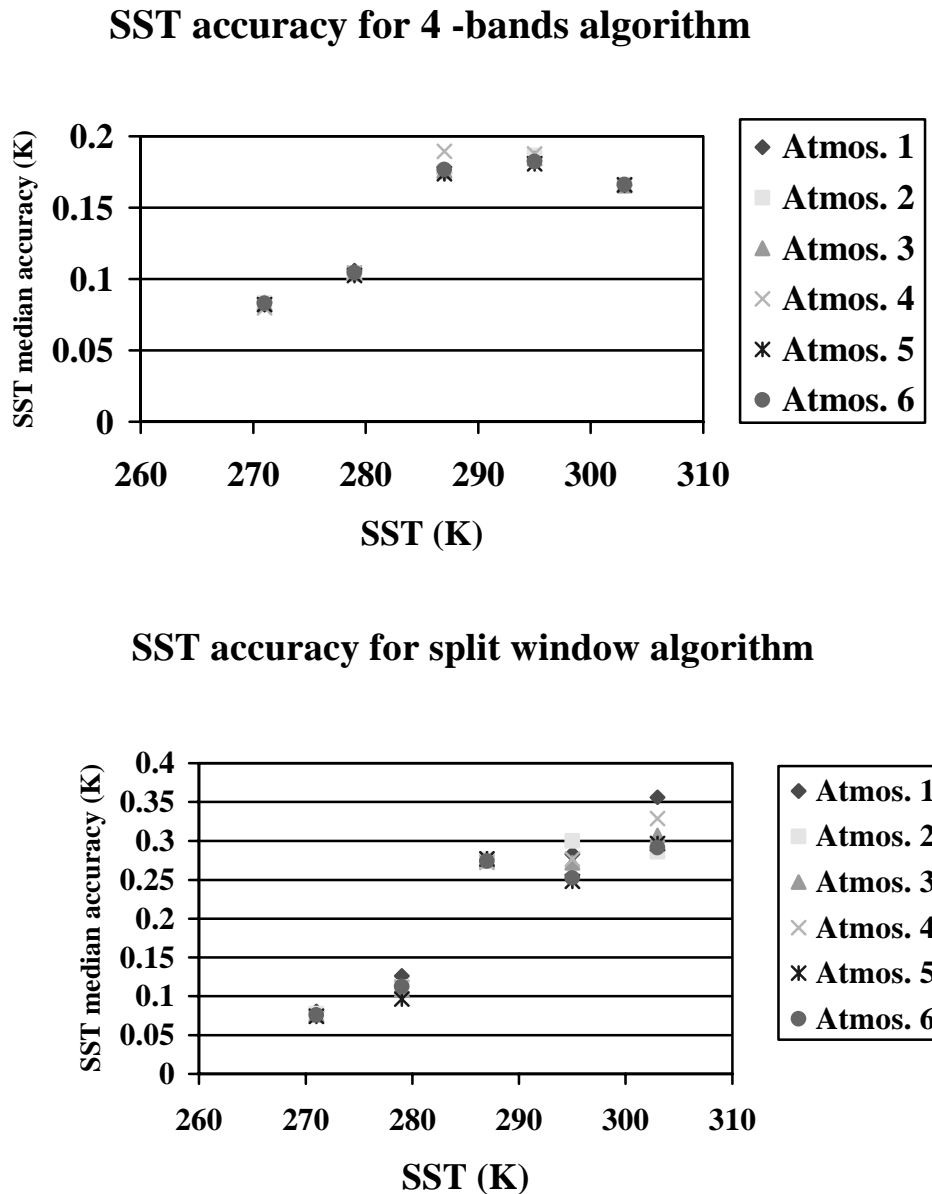


Figure 30. SST RMS accuracy for SBRS 32 perturbation

The retrieved SST accuracy is shown in Figure 31. The RMS accuracy of the VIIRS baseline dual split window algorithm with knowledge of calibration is about 0.17 K (see Figure 31a), below the CAIV target of 0.2 K. The RMS accuracy error of the VIIRS fallback split window algorithm is larger than 0.2 K at warmer temperatures (Figure 31b).

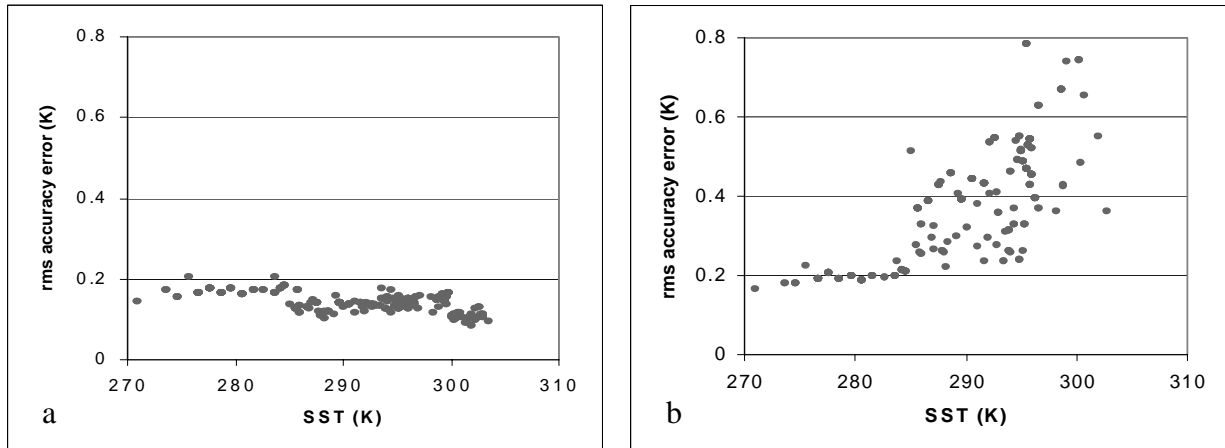


Figure 31. (a) SST RMS accuracy with knowledge of calibration for VIIRS baseline dual split window algorithm, (b) RMS accuracy with knowledge of calibration for VIIRS fallback split window algorithm.

3.4.5 Band-to-Band Registration and Modulation Transfer Function

Figure 32 shows the influence of Band-to-Band Registration (BBR) on the VIIRS fallback split window algorithm precision. The misregistration has significant impact on the retrieval precision when the noise is small. When the sensor noise increases, the influence of BBR becomes less important. Therefore, the BBR is not a critical issue for SST retrieval, especially where the SST gradient is small.

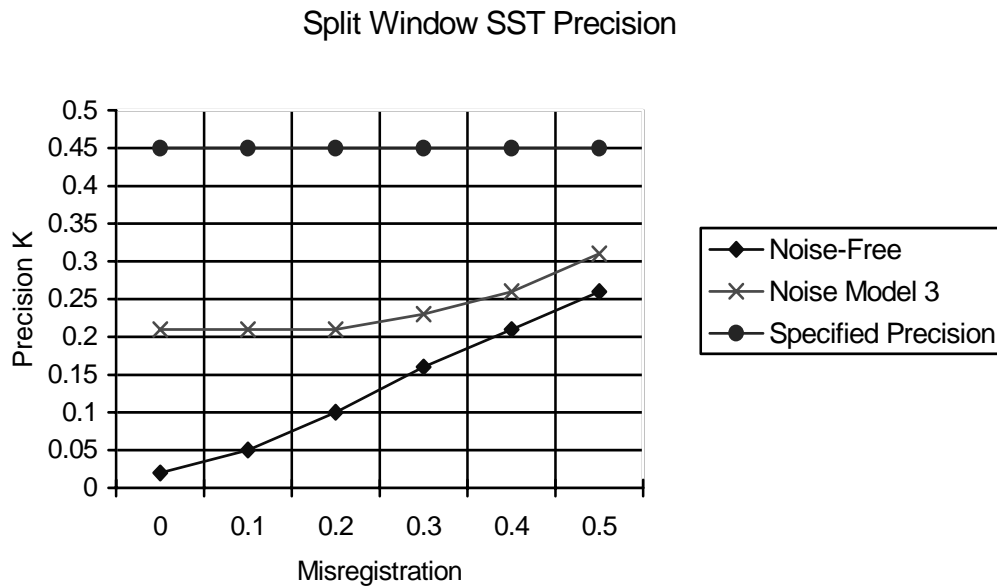


Figure 32. SST precision relevant to BBR.
The misregistration ranges from 0.0 to 0.5 of the pixel area.

Two 1.3-km resolution AVHRR nadir scenes were chosen as SST Modulation Transfer Function (MTF) and BBR test sides. The VIIRS TOA radiances of all VIIRS thermal bands were simulated using radiative transfer model. Only one atmosphere was used in each scene. Therefore the atmospheric correction is near perfect. The data were interpolated into 450 m resolution and a 9-point smoothing was performed to all the data to eliminate the noise.

Figure 33 shows the SST contour plots of scene I (open ocean). Figure 34 shows the SST contour plots of scene II (Gulf Stream Scene). Seven SBRS MTF models were applied to both scenes. The MTF models are circular Gaussian models of MTF, numbered from 1 (sharpest) to 7 (blurriest). Model 1 is 0.7 at Nyquist. Model 7 is 0.1 at Nyquist. Model 3 is 0.5 at Nyquist, (as specified for the imagery bands). Model 5 is 0.3 at Nyquist, (as specified for the moderate bands). The Ground Sampling Distances (GSDs) vary from 150 m to 1250 m. The Horizontal Cell Size (HCS) is 1.3 km. The tests of BBR were performed at GSD level. The data were re-sampled to HCS for all GSDs after MTF models were performed.

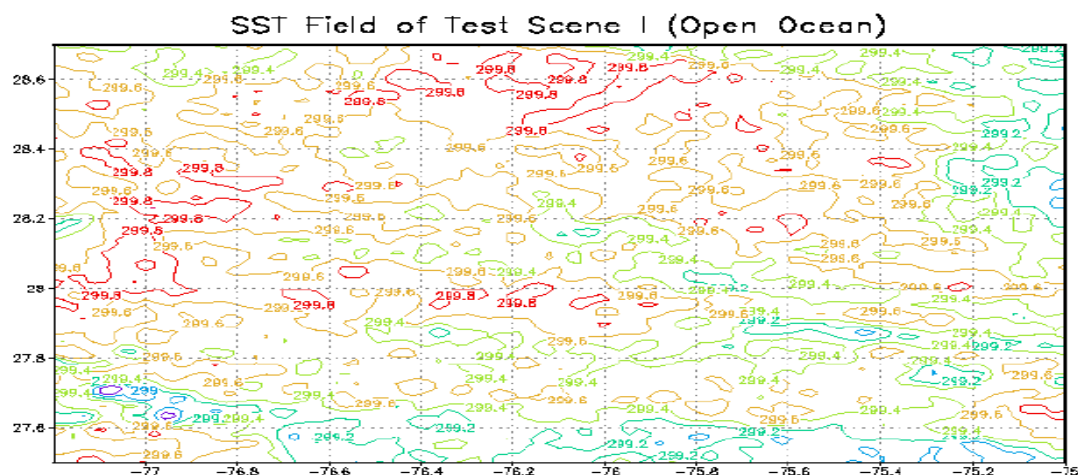


Figure 33. SST fields of Test Scene I (Open Ocean Scene).

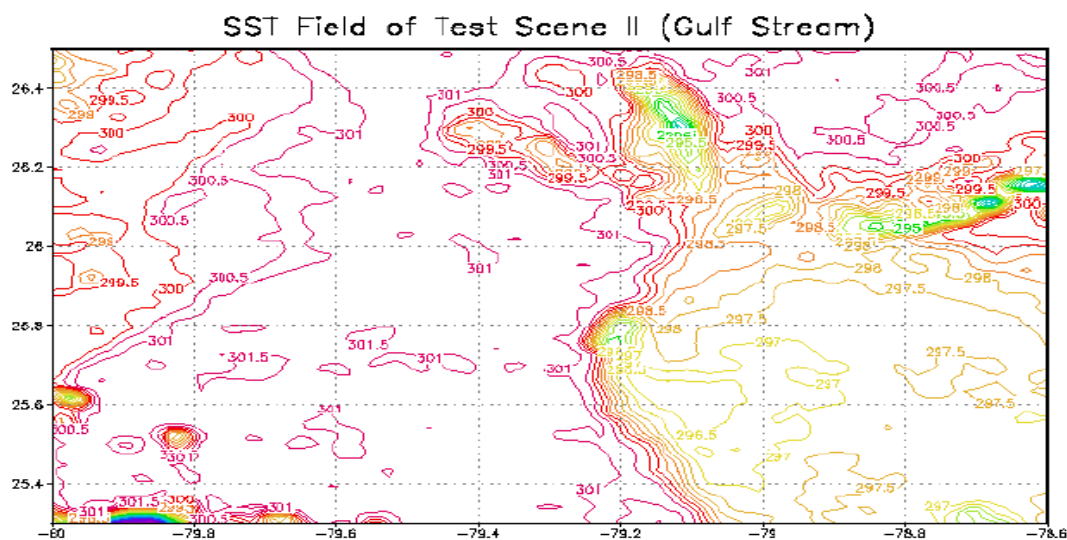


Figure 34. SST fields of Test Scene II (Gulf Stream off Florida).

Figure 35 shows the VIIRS baseline dual split window SST precision for the open ocean scene derived from the seven MTF Models. The error is smaller than 0.015 K. The SST EDR threshold precision requirement is 0.45 K. Therefore, for open ocean, the MTF effect is not important.

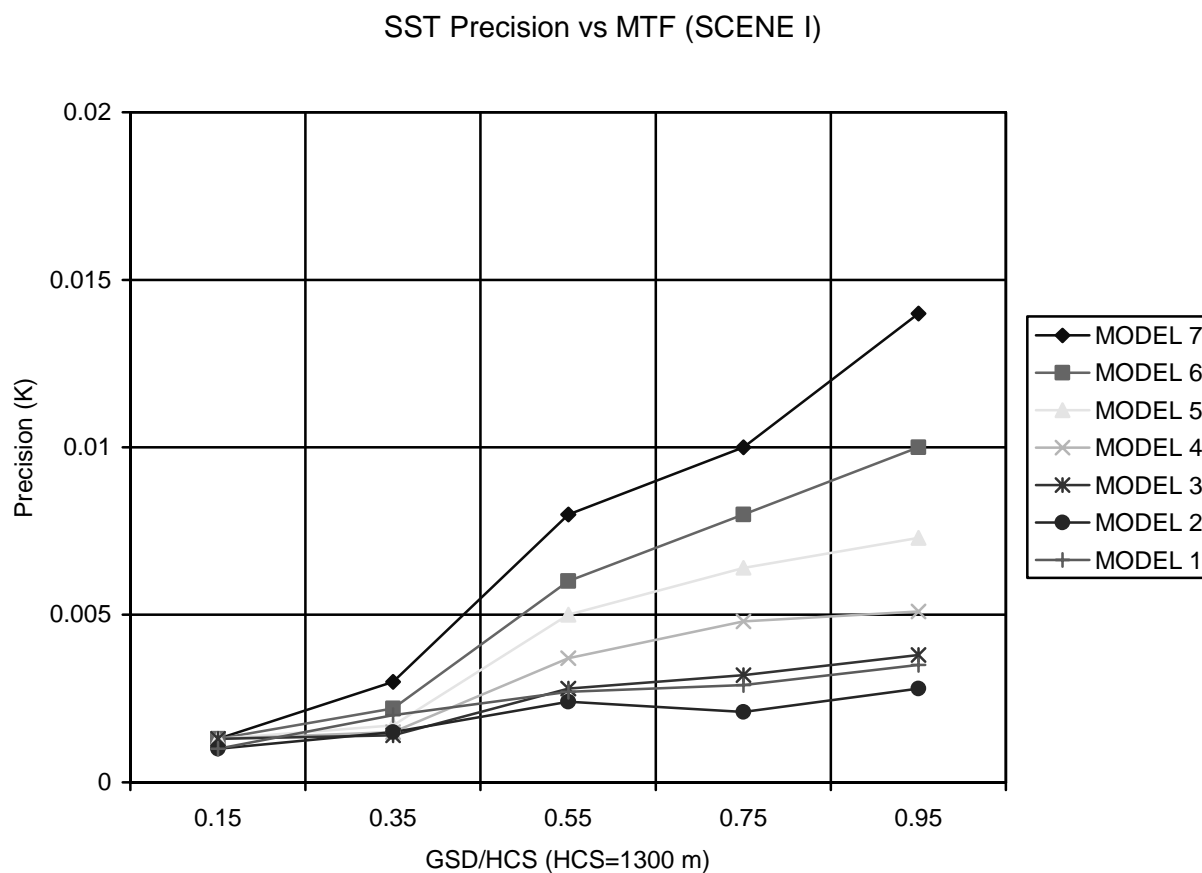


Figure 35. VIIRS baseline dual split window MTF results from open ocean scene.

Figure 36 shows VIIRS baseline dual split window SST precision derived from the seven MTF Models for the Gulf Stream Scene. The maximum error is 0.05 K for Model 7, the model with the worst noise. This is about half of the NEdT value for the 10.8 μm band. To reduce the MTF effects, a model better than model 6 has been baselined. (See the Sensor Specification Document PS154640101.)

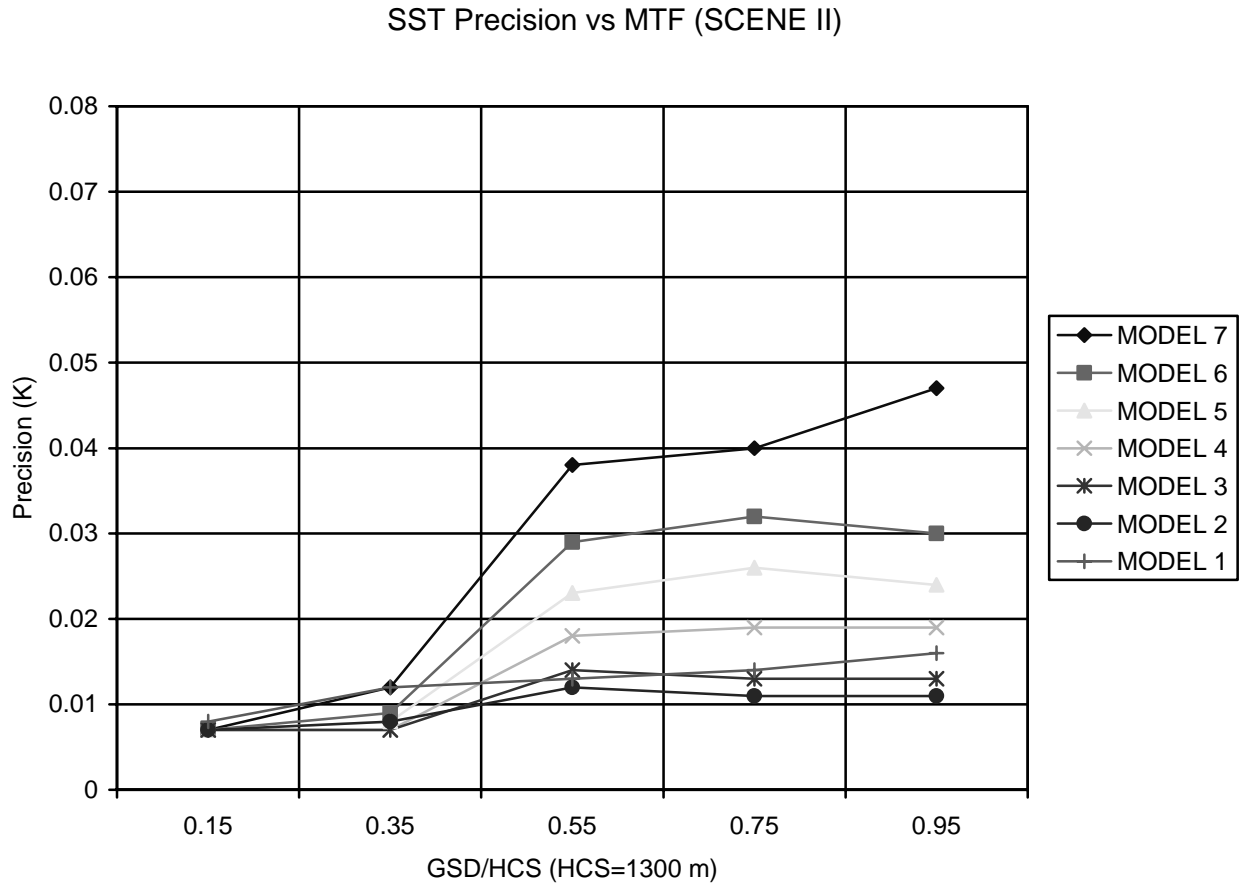


Figure 36. VIIRS baseline dual split window MTF results from Gulf Stream Scene.

Figure 37 shows the VIIRS fallback split window algorithm MTF results from the Gulf Stream Scene. The results do not substantially differ from the VIIRS baseline dual split window solution. In this case, the atmospheric correction is nearly perfectly corrected for both the dual split window algorithm and the split window algorithm.

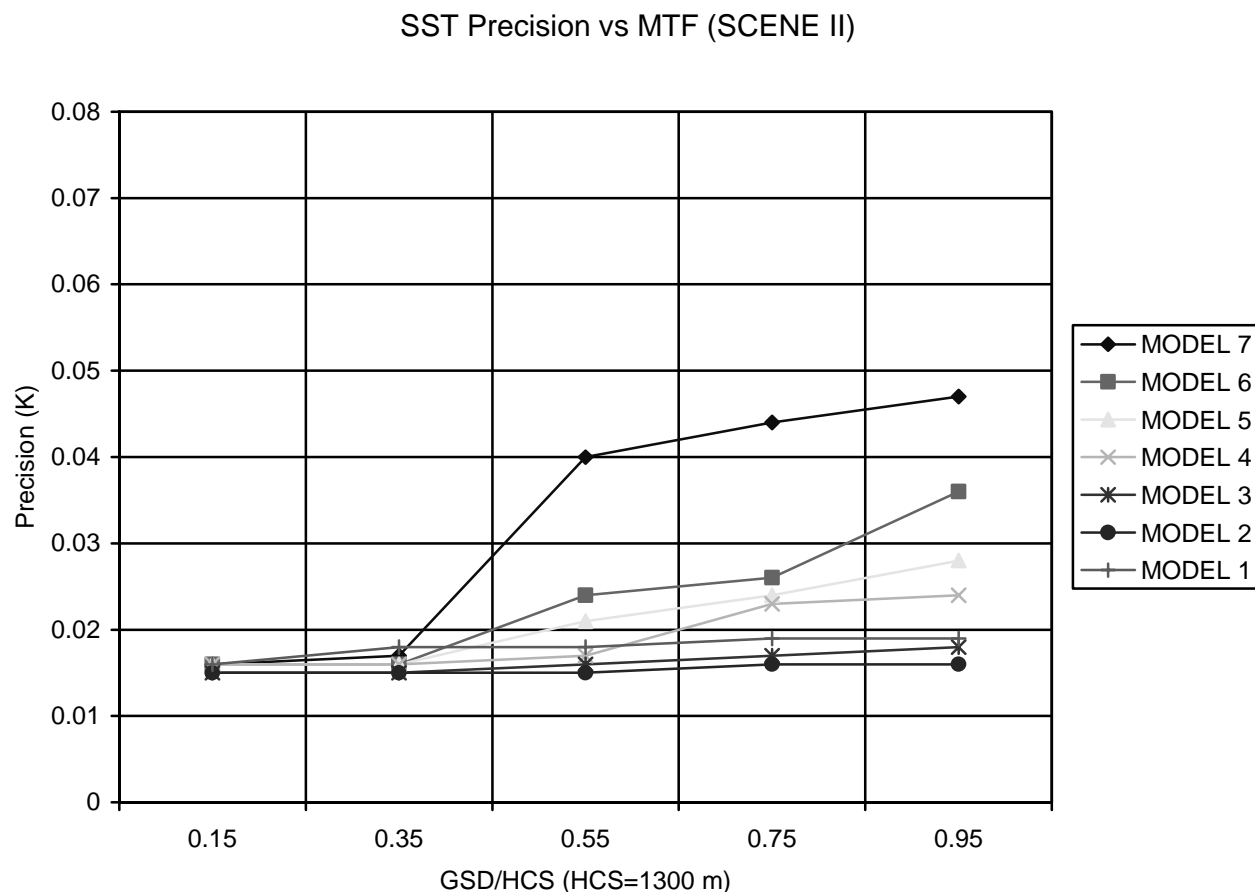


Figure 37. VIIRS fallback split window MTF results from Gulf Stream Scene.

Figure 38 shows the combined effects of BBR and MTF effects for the open ocean scene for the VIIRS baseline dual split window algorithm. The MTF model is SBRS Model 3. The precision at worst case (GSD=HCS, misregistration =50%) is about 0.02 K. The precision is about 0.01 K at GSD/HCS ratio of 0.6 and misregistration of 35%. This result indicates that for the open ocean, BBR and GSD/HCS ratio do not drive SST error.

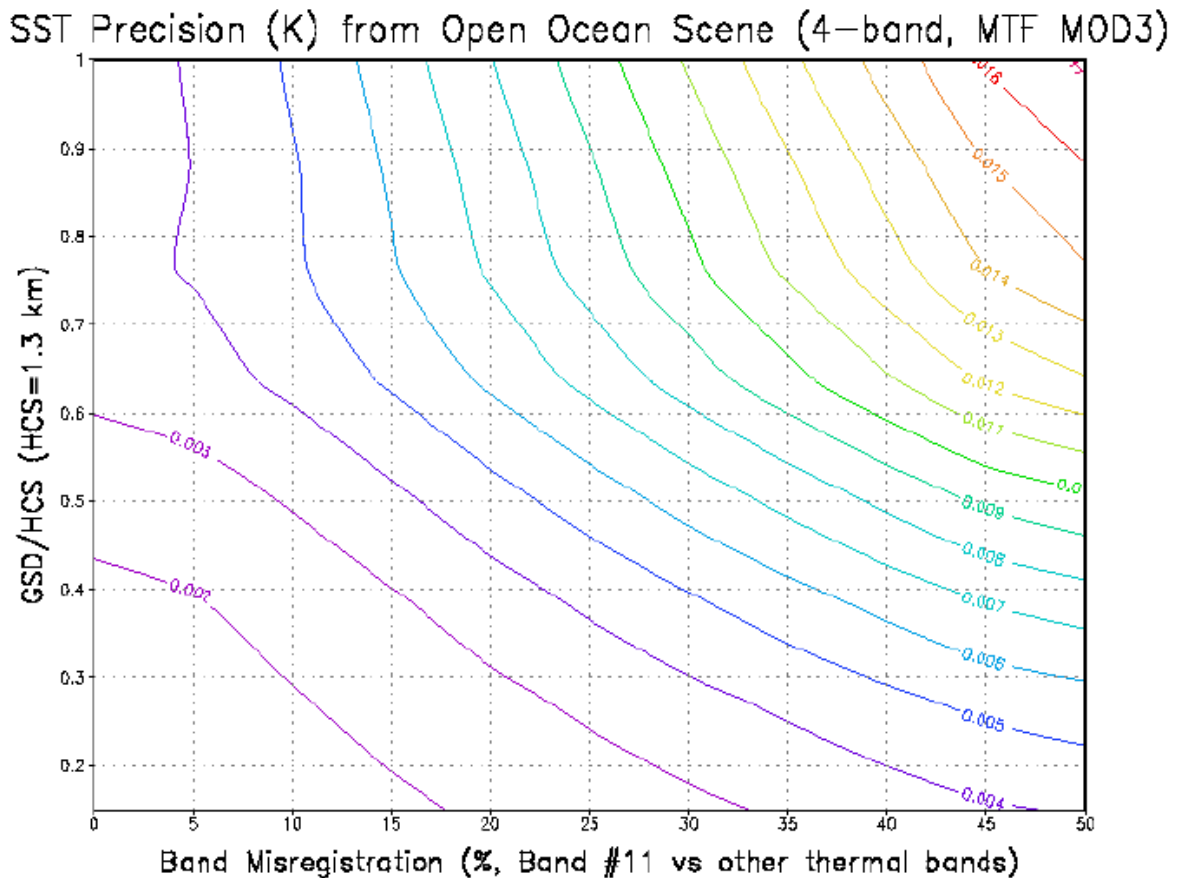


Figure 38. The combined effects of BBR and MTF on the VIIRS baseline dual split window SST algorithm for open ocean scene.

Figure 39 shows the combined effects of BBR and MTF effects for the Gulf Stream Scene for the VIIRS baseline dual split window algorithm. The MTF model is SBRS Model 3. The results show that the precision varies from 0.02 K to 0.3 K within a misregistration range of 0% to 50%. The effect of larger misregistration ($> 30\%$) and large GSD/HCS (> 0.6) is significant compared to the total error budget of about 0.3 K for this algorithm. The precision is 0.12 K at GSD/HCS=0.6 and misregistration of 30%. The SST error budget for BBR and MTF effects is 0.1-0.15 K. Therefore, the sensor meets requirements for GSD/HCS <0.6 and misregistration $< 35\%$.

SST Precision (K) from Gulf Stream Scene (4-band, MTF MOD3)

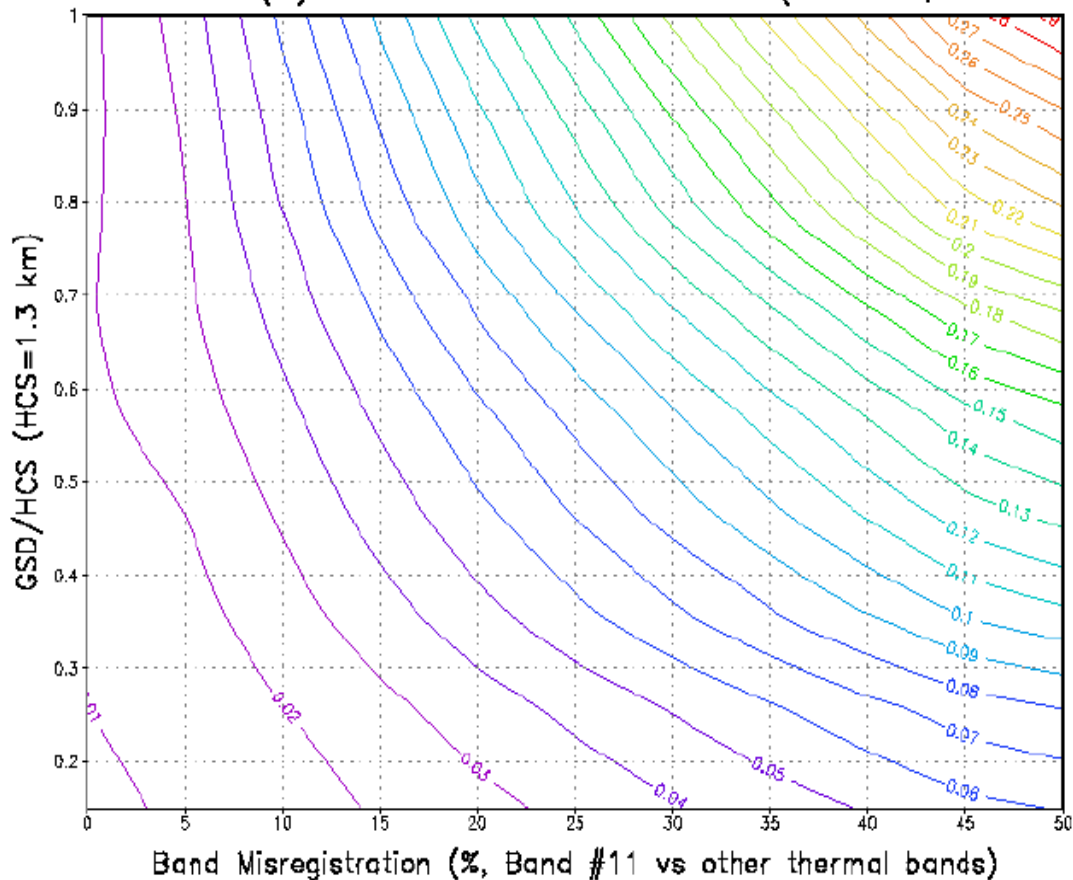


Figure 39. The combined effects of BBR and MTF on VIIRS baseline dual split window SST algorithm for Gulf Stream scene.

Figure 40 shows the combined effects of BBR and MTF effects for the Gulf Stream Scene for the VIIRS fallback split window algorithm. The MTF model is SBRS Model 3. The precision is better for the cases with small misregistration and GSD/HCS ratio.

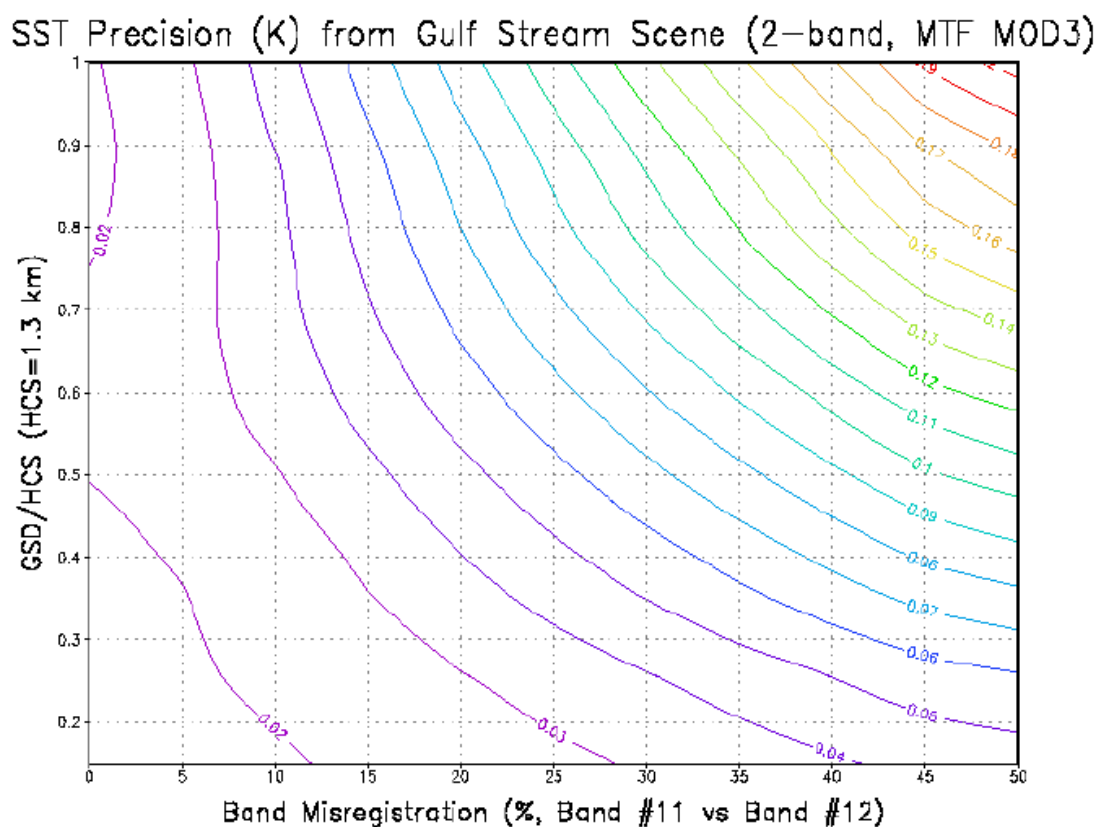


Figure 40. The combined effects of BBR and MTF on split window SST algorithm for Gulf Stream scene.

3.5 PRACTICAL CONSIDERATIONS

3.5.1 Numerical Computation Consideration

In order to retrieve SST within an operational timeframe, statistical algorithms that meet quality requirements have been developed that are much quicker than physical modeling methods. Pre-generated LUTs are used to speed processing yet retain flexibility.

3.5.2 Programming and Procedural Considerations

The simplicity of all the algorithms described in this document translates into very small amounts of code using basic mathematical routines. Computationally intensive processes are performed offline, with results delivered as re-generated LUTs. VIIRS Phase II efforts are largely software-focused, and the methodology for this development work is based on sound and proven principles, as discussed in the VIIRS Algorithm Software Development Plan [Y6635]. The present maturity of the VIIRS software is detailed in the VIIRS Algorithm Software Maturity Assessment document [Y6661]. The maturity and remaining Phase II tasks for the algorithms themselves is summarized in the VIIRS Algorithm/Data Processing Technical Report [Y7040]. The software designs relevant to the SST Unit are summarized in the VIIRS Context Level Software Architecture [Y2469], Surface Temperature Module Level Software Architecture [Y2473], and Sea Surface Temperature Unit Level Detailed Design [Y2504]. These designs are tested at the system level as described in the most recent versions of the VIIRS Software Integration and Test Plan [Y3236], Algorithm Verification and Validation Plan [Y3237], and System Verification and Validation Plan [Y3270]. A summary of the ultimate strategy for operational application of the system of VIIRS algorithms is provided in the VIIRS Operations Concept document [Y2468]. The VIIRS Interface Control Document (ICD [Y2470]) provides more detail on the specifics of ancillary data requirements for Vegetation Index and other VIIRS products.

3.5.3 Configuration of Retrievals

Adjustable parameters for the retrieval of the SST products allow selection of atmospheric classifications, separate selection of retrieval algorithms for skin SST and for bulk SST. The flexibility built into the architecture also allows easy implementation of future P³I developments.

3.5.4 Quality Assessment and Diagnostics

A number of parameters and indicators are reported in the SST product as retrieval diagnostic flags. Statistical information is reviewed for quality assessment. Table 6 lists the available quality flags. The final list of delivered flags will be determined in the operational environment.

Table 6. VIIRS SST EDR Quality Flags

Byte	VIIRS SST Flag	Result	Bits
1	Land / Water Background	000 = Land & Desert 001 = Land no Desert 010 = Inland Water 011 = Sea Water 100 = Coastal	3
	Skin SST quality	11 = Good 10 = Probably Good 01 = Probably Poor 00 = Poor	2
	Bulk SST quality	11 = Good 10 = Probably Good 01 = Probably Poor 00 = Poor	2
	Aerosol Correction	1 = Corrected 0 = Not Corrected	1
2	Skin SST Algorithm	1 = Split Window 0 = Dual Split Window	1
	Bulk SST Algorithm	1 = Split Window 0 = Dual Split Window	1
	SST State	11 = Cool 10 = Warm Unclassified 01 = Warm Dry 00 = Warm Moist	2
	Cloud Detection Result & Confidence Indicator	11 = Confident Cloudy 10 = Probably Cloudy 00 = Confident Clear 01 = Probably Clear	2
	Snow / Ice Surface	1 = Snow/Ice 0 = No Snow/Ice	1
	Day / Night	0 = Night 1 = Day	1
3	Non Cloud Obstruction (Heavy Aerosol)	1 = Yes 0 = No	1
	Fire Detected	1 = Yes 0 = No	1
	Thin Cirrus Detection (Solar) (RM9)	1 = Cloud 0 = No Cloud	1
	Thin Cirrus Detection (IR) (BTM15-BTM16)	1 = Cloud 0 = No Cloud	1
	IR Threshold Cloud Test (BTM15)	1 = Cloud 0 = No Cloud	1
	High Cloud (BTM12 - BTM16) Test	1 = Cloud 0 = No Cloud	1
	IR Temperature Difference Test (BTM14 - BTM15 & BTM15 - BTM16)	1 = Cloud 0 = No Cloud	1
	Temperature Difference Test (BTM15 - BTM12)	1 = Cloud 0 = No Cloud	1

Byte	VIIRS SST Flag	Result	Bits
4	Temperature Difference Test (BTM12 – BTM13)	1 = Cloud 0 = No Cloud	1
	Visible Reflectance Test (RM5)	1 = Cloud 0 = No Cloud	1
	Visible Reflectance Test (RM7)	1 = Cloud 0 = No Cloud	1
	Visible Ratio Test (RM7/RM5)	1 = Cloud 0 = No Cloud	1
	Sun Glint	00 = None 01 = Geometry Based 10 = Wind Speed Based 11 = Geometry & Wind	2
	Adjacent Pixel Cloud Confident Value	11 = Confident Cloudy 10 = Probably Cloudy 00 = Confident Clear 01 = Probably Clear	2

3.5.5 Exception Handling

Pixels identified by the cloud mask as confident cloudy are not processed.

3.6 ALGORITHM VALIDATION

3.6.1 Pre-Launch Validation

The atmospheric correction algorithm will be derived pre-launch by radiative transfer modeling to simulate the VIIRS TIR channel measurements. Selected radiosondes from the operational network stations or field campaigns will be used in the VIIRS simulations for the development of the atmospheric correction algorithm. Measurements from the operational surface drifting and fixed buoy programs will be used to characterize the surface temperature fields and to validate the atmospheric correction algorithms. The assimilated meteorological fields provided by NCEP and ECMWF provide a valuable description of the marine atmosphere and surface temperature. These fields will be used in conjunction with the radiative transfer modeling to simulate the VIIRS measurements in order to validate the radiosonde data and to provide direct input to the radiative transfer modeling process.

Measurements from AVHRR and ATSR will be used in the pre-launch phase to study the error characteristics of the SST retrieval.

To date, the requirements for this EDR are for retrieval of skin SST. However, both skin SST and bulk SST can be retrieved using the same algorithm forms. Currently, the baseline VIIRS algorithm is a dual split window retrieval using two MWIR bands and two LWIR bands. When sun glint prevents the use of the MWIR bands, the software architecture is designed to fall back to the LWIR split window algorithm. Pre-launch, the coefficients for skin retrieval will be derived from *in situ* radiometric measurements and from other physical retrievals such as ATSR.

The coefficients for bulk retrieval will be derived from buoy and other bulk measurements, and from retrievals such as AVHRR.

3.6.2 Post-Launch Calibration and Validation

It is important to recognize the definitions of bulk and skin SST. Radiometric sensors measure radiance from only the skin of the ocean. Bulk SST corresponds to the temperature of the upper layer of the ocean, and is measured below or through the skin layer using methods such as ship injection flow-through systems, buoys, etc.. Bulk SST has been used in the development of air-sea heat exchange formulae generally known as the bulk formulae.

In the calibration process we acknowledge that the IR sensor will drift, and that there are problems with atmospheric corrections driving us to provide for coincident *in situ* measures of the SST so that we can compute the SST algorithm coefficients by comparison to these “truth” measurements. At the present time, we do not have sufficient *in situ* skin SST measurements to calibrate the skin SST algorithm coefficients. Calibrating satellite skin SST with *in situ* measures of bulk SST results in SST errors of 0.3 - 1.0 K. Although it is true that errors due to atmospheric effects can overwhelm this error, it is one that is well known and easy to correct for. The atmosphere errors change considerably in both time and space, and methods are still being developed to improve on these corrections.

At present we use “atmospheric simulations” to compute the coefficients for the skin SST algorithms. Here we use a selected set of radiosonde and a radiative transfer model to “synthesize” the skin SST as the lowest layer temperature in our model. Recent experience with these types of skin SST has demonstrated that the skin SST is too warm by a significant amount.

Only *in situ* skin SST measurements will reduce uncertainty and inaccuracy in calibrating skin SST. The same problems affect accurate validation of skin SST retrievals.

It will be necessary to establish global or at least meridionally distributed programs of bulk and skin measurements for post-launch validation and updating of coefficients. What is needed is a large number of TIR radiometers installed on moored buoys and ships of opportunity that routinely collect skin SST measurements. Along with these radiometric skin SSTs we need to collect a range of other supporting parameters. We need to measure the simultaneous bulk SST, which can be done with a thermistor attached to the inside of the ship's hull. In addition, it is useful to record as many of the standard parameters of the bulk fluxes such as wet-bulb temperature, air temperature, wind speed, and cloud cover. Water vapor attenuation can be measured with coincident measurements of the total column atmospheric moisture, which can be made by passive microwave instruments.

Various groups are now developing radiometer systems that can be installed on ships of opportunity or on moored buoys. These systems are being designed to operate autonomously and report by satellite, giving us a real time set of skin SST measurements. All of these buoy and ship installations will also provide us with bulk SST and most of the heat flux parameters. It is

not yet clear what these instruments will cost, and this uncertainty makes it difficult to estimate the cost of operating these units. At present the best guess is that the ship-of-opportunity units will cost about \$10,000, and that the buoy units will probably cost about \$25,000. Research versions of these instruments run between \$50,000 and \$250,000 depending on the overall character of the instruments.

Because NPOESS is a global sampling platform, it is necessary to collect measurements over the entire globe. For this discussion it will be assumed that the United States must be responsible for the collection and reduction of these measurements. It may prove possible to distribute this responsibility among the various nations using data from the NPOESS system. It is easier for these other countries to maintain a measurement network located in their region. To start with, we need to select ship-of-opportunity routes that cover large parts of the ocean. Typical are the ships that travel regularly between the West Coast of the United States and Australia/New Zealand. Other ships go from the East Coast (i.e., Boston) and travel through the Panama Canal to Japan and China. In the Atlantic, there are ships that travel from Europe and the United Kingdom down to South America and the Falkland Islands. Other long shipping lines crisscross the Indian Ocean and the South Atlantic. Data from these long lines must be transferred back via satellite to be useful for the routine calibration of the satellite radiance data. This can be done either via the DCS system on NPOESS or by using geostationary weather satellites.

For NPOESS to start its own moored buoy program would be expensive and logistically difficult, and at present a number of buoys are already being operated by various Government agencies. These existing moored buoys should be the primary target of the NPOESS SST validation effort. The deployment of moored buoy skin SST radiometers should be made so as to optimize the spatial distribution of skin SST measurements. Here again, it should prove useful to work with other countries that are likely to operate their own suite of moored buoys for various reasons. It is a challenge to start a new moored buoy activity, and everything possible should be done to marry the NPOESS effort with existing projects.

We need to be very clear on the differences between calibration and validation. The former is used to correct errors in the sensor and the corrections. The assumption is that the *in situ* measurements are “correct” and that the VIIRS radiance measurement must be adjusted to fit the *in situ* data. It is important to have some idea as to how representative the *in situ* data are of the true skin SST. The validation data, on the other hand, are intended to demonstrate how well the sensor and algorithms have performed up to the specifications given for the VIIRS. It is critically important to use a different set of data for calibration and validation. That is not to say that they shouldn’t be the same kind of data but that they should be different individual measurements. Thus, the calibration data can be from one period of measurements while the validation data are from a completely different period. There is some danger that longer time-scale variability will influence this comparison, but this is generally not a problem. It is assumed that the data used for validation are statistically independent of the calibration measurements, which in the past was not always true with SST. It is important to have sufficient calibration measurements to have statistically significant results. There must also be sufficient validation measurements to yield usefully significant results. Unlike the calibration measurements, the validation system must operate continuously to be able to assess and update the satellite data. For this reason we propose a plan that can be continuously maintained to provide validation information over the

life of NPOESS. Whether the operation of this validation network is maintained by the NPOESS operators or by an independent contractor must be decided before the system is initiated.

It is assumed that NPOESS and its instruments represent the latest in technology at the time of creation. Thus, we can expect greater precision and accuracy with all of the instruments including the VIIRS. One might think that with these greater accuracies it should be possible to reduce or perhaps eliminate the *in situ* calibration/validation part of the project. Experience has shown us, however, that all new instruments behave slightly differently than expected, making the need for *in situ* cal/val data even greater than it has been with previous programs. In fact, the higher accuracies of the NPOESS instruments dictate that the *in situ* measurements yield an even higher accuracy themselves in order to act as a reference for the satellite data. This means that the *in situ* measurements have to be more accurate, requiring better instruments and much greater care in their operation. Thus, the NPOESS era calibration/validation measurements must be considerably better than our present capabilities. Present work in IR detectors and in instrument cooling systems suggest that these accuracies and reliabilities should be available in the next 4 or 5 years. These new capabilities should make it possible to have *in situ* reference measurements accurate to about 0.05 K.

There are a number of large buoys deployed around the U.S. to monitor weather changes constantly and assist in such operations as the shipment of oil from Alaska to the lower states. There are also buoys in the so-called TAO array marked by a rectangle around the equator. The buoys in the TAO array and other moored buoys relay their information by satellite providing realtime access to these data. Skin SST radiometers are being developed to operate autonomously from these buoys. Thus we include them in our validation sampling plan. Between now and the implementation of NPOESS, this buoy array may have changed considerably, but the expectation is that it will only increase the number of buoys deployed and operated. It is hoped that many of these buoys will operate in regions where ship-of-opportunity measurements are relatively few.

3.7 ALGORITHM DEVELOPMENT SCHEDULE

During this period, SST algorithms are mainly used to flowdown the sensor requirements. It is expected that this algorithm will be completed within 2-3 years.

4.0 ASSUMPTIONS AND LIMITATIONS

4.1 SENSOR PERFORMANCE

The VIIRS SST retrieval is done under clear sky conditions. Another limitation is the limitation of swath angle. As discussed in section 3.3.4, the retrieval uncertainty becomes much larger at swath angles larger than 40°. The swath width used for SST retrieval will be only the center 2000 km of the swath.

4.2 P³I

4.2.1 Aerosol Correction by AOT and Aerosol Type

The VIIRS baseline SST algorithm meets requirements for 99% of global scenes. However, it is generally known that high aerosol loads present an additional problem for SST retrieval. This problem has been discussed by McClain (1989), Griggs (1985), May *et al.* (1992) and others. The basic method in these studies was to find an empirical equation that relates AOT to the SST change in the retrieval and to correct this change to get a more realistic SST. May *et al.* (1992) found that the correction is well correlated with $\tau \sec(\theta)$, where τ is the AOT and θ is the satellite zenith angle.

This section evaluates the error contribution due to volcanic eruption. The data used are from a "training data set" (MODTRAN simulations from real global aerosol fields of monthly AOT) using 225 skin SSTs and atmospheric profiles. For each skin SST, we made 225 simulation for 9 satellite zenith angles, 5 solar zenith angles, and 5 AOT values. These simulations were used to establish the relationship between brightness temperatures and aerosol thickness as well as zenith angles. Following the paper by May *et al.* (1992), the SST change is linearly related to $\tau \sec(\theta)$. In this work, we assume the change of brightness temperatures are linearly related to $\tau \sec(\theta)$, i.e.

$$T_b = a T_{ba} + b \tau \sec(\theta) \quad (15)$$

Where T_{ba} is the brightness temperature when aerosol exits, T_b is the corrected brightness temperature.

The procedure is as follows: calculate brightness temperature for each band, using above equation to correct brightness temperature, before using the SST algorithm to perform SST retrieval.

Figure 41 shows three results from the VIIRS baseline dual split window SST algorithm. The red line shows the accuracy of SST retrieval without correction. The accuracy is ~0.4 K when $\tau=0.4$ and ~2.2 K at $\tau=0.8$. This indicates that a small change of optical thickness will introduce large SST error if uncorrected. The purple line indicates perfect correction, i.e. the optical thickness in testing data is the same as those in training data. The green line shows the results from our current aerosol brightness temperature correction algorithm described above. The blue line shows the results using an SST correction method adopted from May *et al.* (1992). The

mean bias was almost removed using both correction methods. Figure 42 shows the nighttime SST accuracy. However, AOT cannot be determined operationally at night.

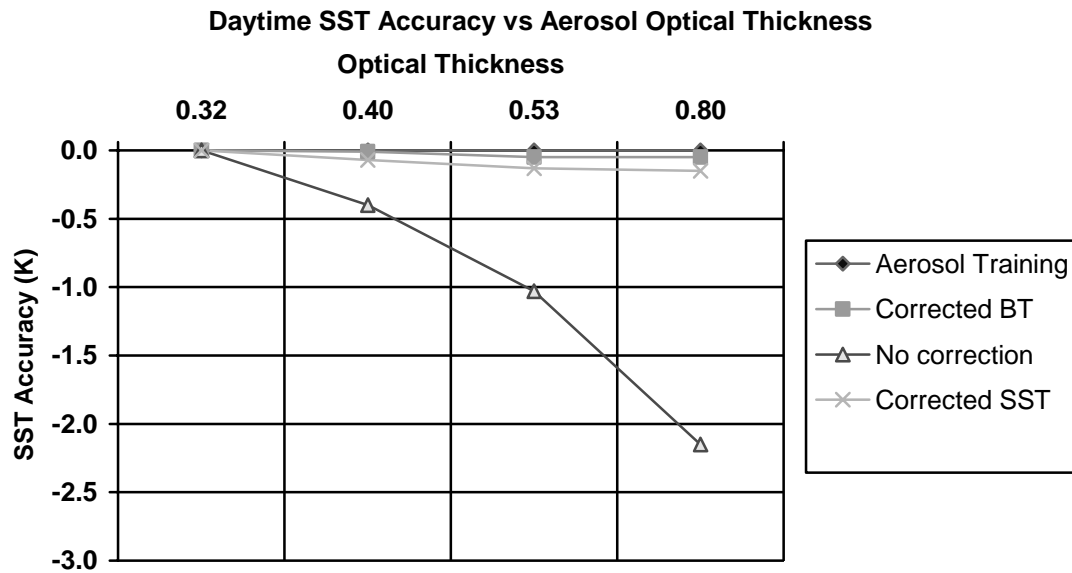


Figure 41. Daytime SST accuracy as a function of optical thickness in testing data

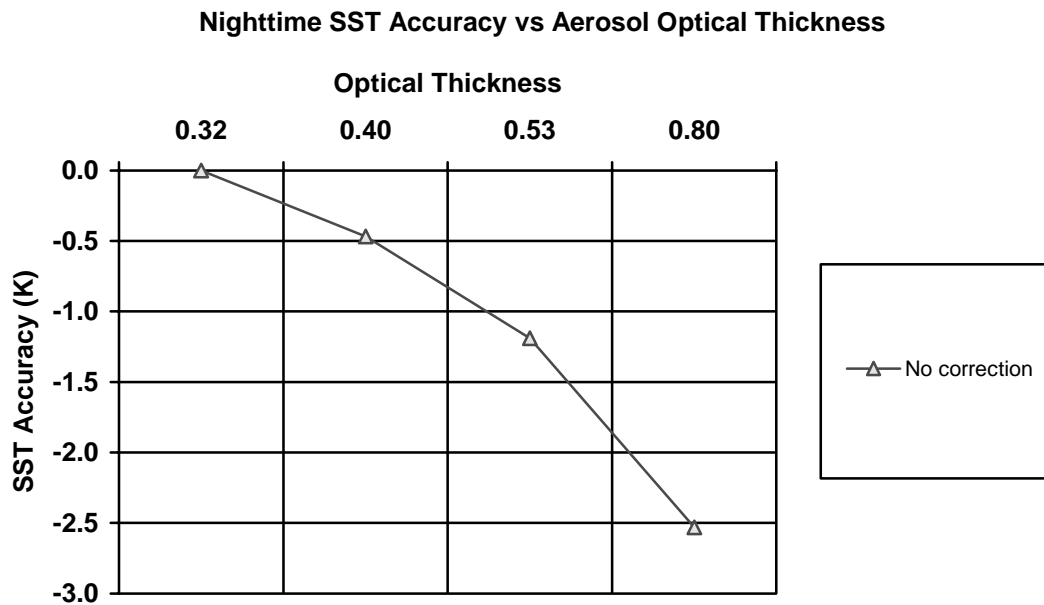
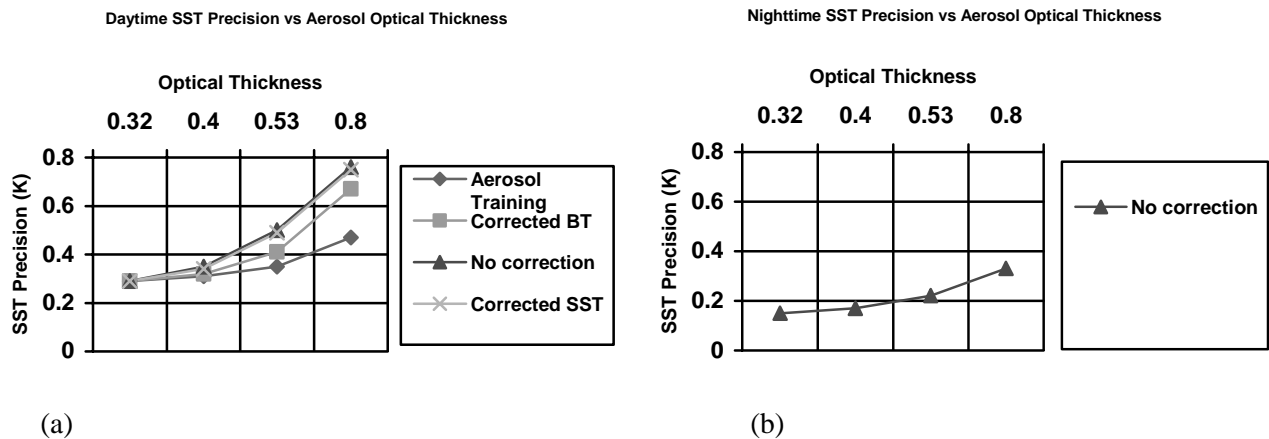


Figure 42. Nighttime SST accuracy as a function of optical thickness in testing data.

Figure 43 shows the precision as a function of optical thickness. The error increases when optical thickness becomes larger even for perfect correction. Using the brightness temperature correction method, the error is reduced to the threshold value (0.45 K) when optical thickness is less than 0.53. Figure 43(b) is the nighttime SST precision. The aerosol does not cause large precision error during nighttime.



**Figure 43. (a) SST precision as a function of AOT.
(b) Nighttime SST precision as a function of AOT.**

In above figures, the aerosol height and type do not vary. Figure 44 shows the SST accuracy as a function of AOT in two cases:

1. Aerosol concentrated between 0-4 km height
2. Aerosol concentrated between 4-8 km but the aerosol type is the same as in case 1

The results show that, if only aerosol height changes for volcanic aerosol, the error does not increase significantly.

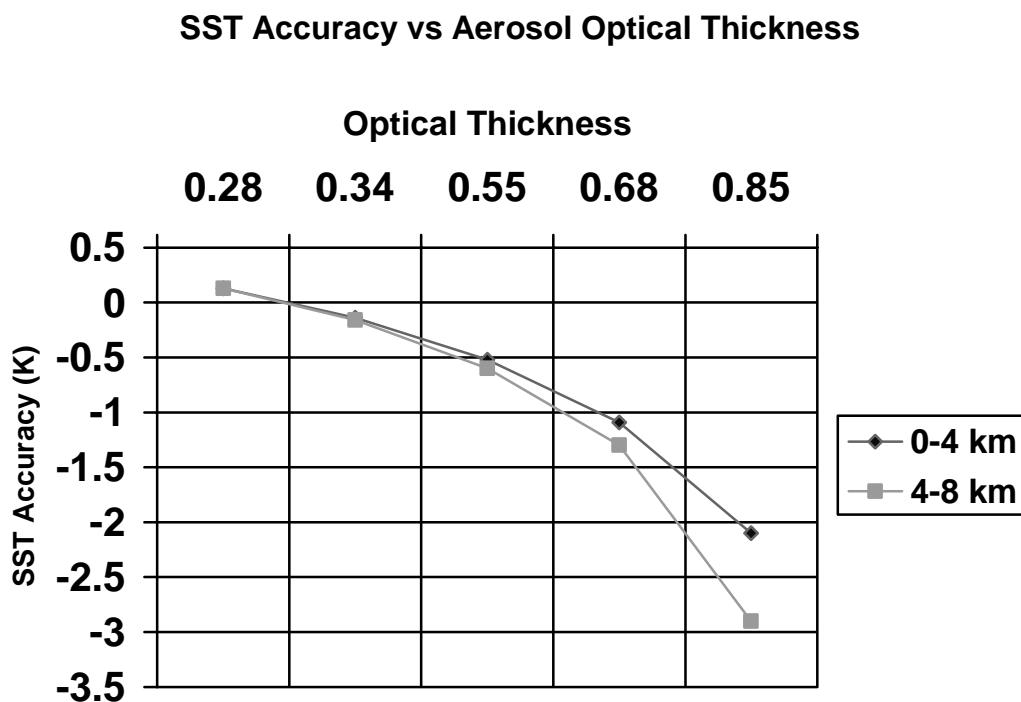


Figure 44. SST accuracy as a function of optical thickness and aerosol heights.

Further simulations were performed with NCEP July 1998 reanalyzed data, with a correction based on AOT. The AOT is from NESDIS data, derived from the AVHRR data. Figure 45(a) shows the AOT distribution. Figure 45(b) shows the retrieved SST bias without aerosol correction, Figure 45(c) is the bias distribution after aerosol correction to the brightness temperature, Figure 45(d) shows the bias distribution after perfect correction. SST bias are as large as -0.8 K without correction. However, the large bias are reduced significantly after correction (see Figure 45c).

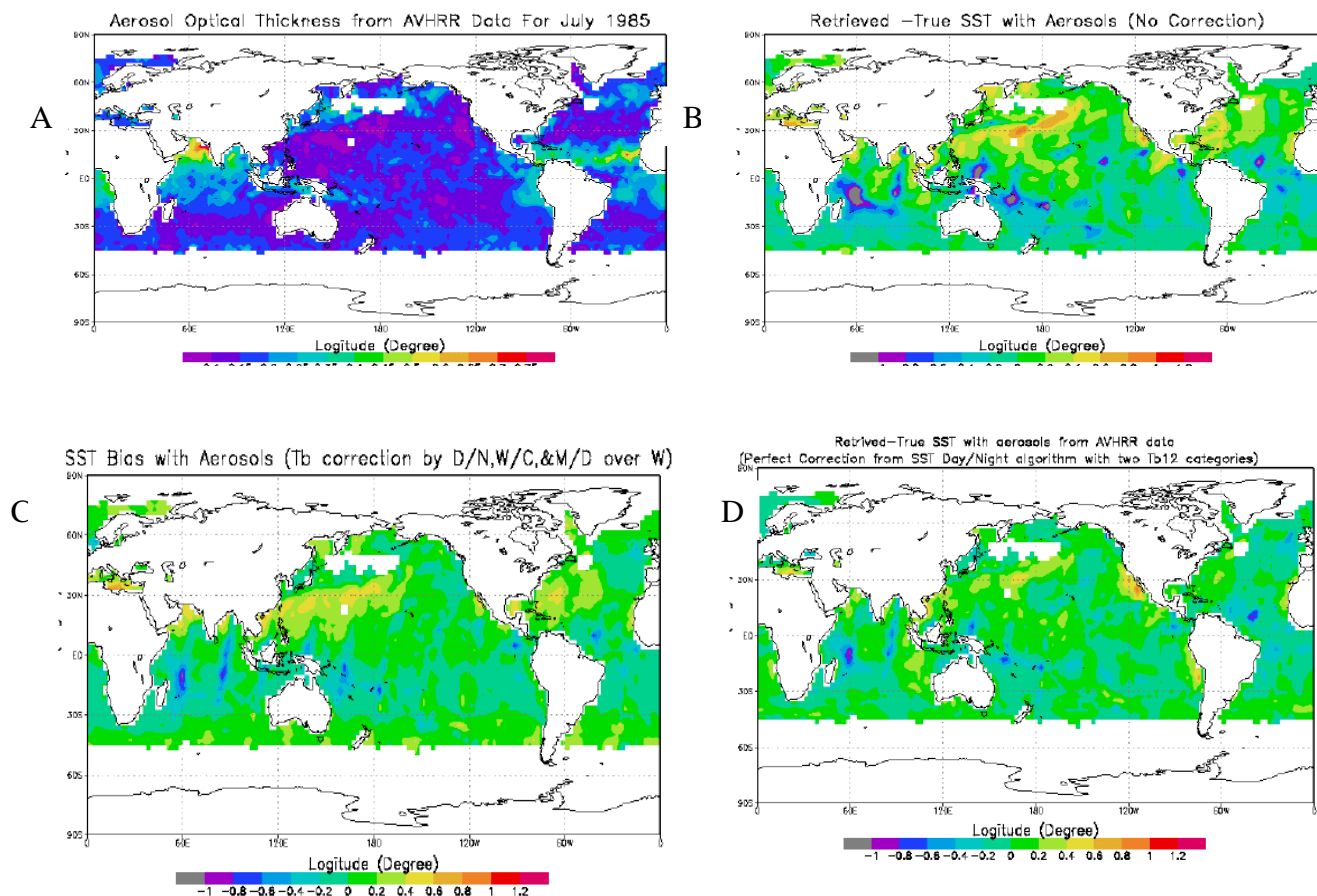


Figure 45. (a) AOT distribution. (b) Retrieved SST bias without aerosol correction. (c) SST bias after aerosol correction to brightness temperature. (d) SST bias after aerosol correction.

In order to consider the effect of aerosol type in addition to AOT's effect, four aerosol types specified as rural, urban, maritime, and desert were determined for the NCEP July 1998 reanalyzed data. Aerosol type was varied in the training data set, with a correction based on AOT.

The SST bias is shown as Figure 46(b). The cloud type in the simulation is shown in Figure 46(a), including 1) cumulus, 2) altostratus, 3) stratus, 4) stratus/stratocumulus, and 5) nimbostratus. Figure 46(b) shows that if the effects of aerosol type are not considered, the SST precision error can be as large as 0.9 K and the accuracy error can be as large as -0.8 K. After

considering the effect of aerosol type, a precision of 0.22 K is obtained and the accuracy error is reduced to < 0.1 K with a few exceptions.

The effect of aerosols on SST retrieval varies with aerosol type, optical thickness, altitude and temperature. To compensate for these variable and episodic effects, two types of corrections have been designed into the software architecture. For optically well characterized aerosols, such as aged volcanic ash, LWIR and MWIR brightness temperatures are corrected based on AOT, as described in equation 15. This is implemented as an enhancement to the VIIRS baseline and fallback algorithms. For variable aerosols, such as dust transport or fresh volcanic injection, aerosol type and AOT are determined by the VIIRS aerosol algorithms.

For P³I implementation, these can be used as factors in the regression and selection of coefficients for the SST retrieval algorithms. This type of data can be derived from MODIS and other sources for pre-launch characterization, and it should be derived post-launch from VIIRS retrievals for use as factors in the regression and selection of coefficients for the SST retrieval algorithms.

In this way, aerosol characteristics that are retrievable by the VIIRS aerosol algorithms can be used to tune the SST retrieval algorithms.

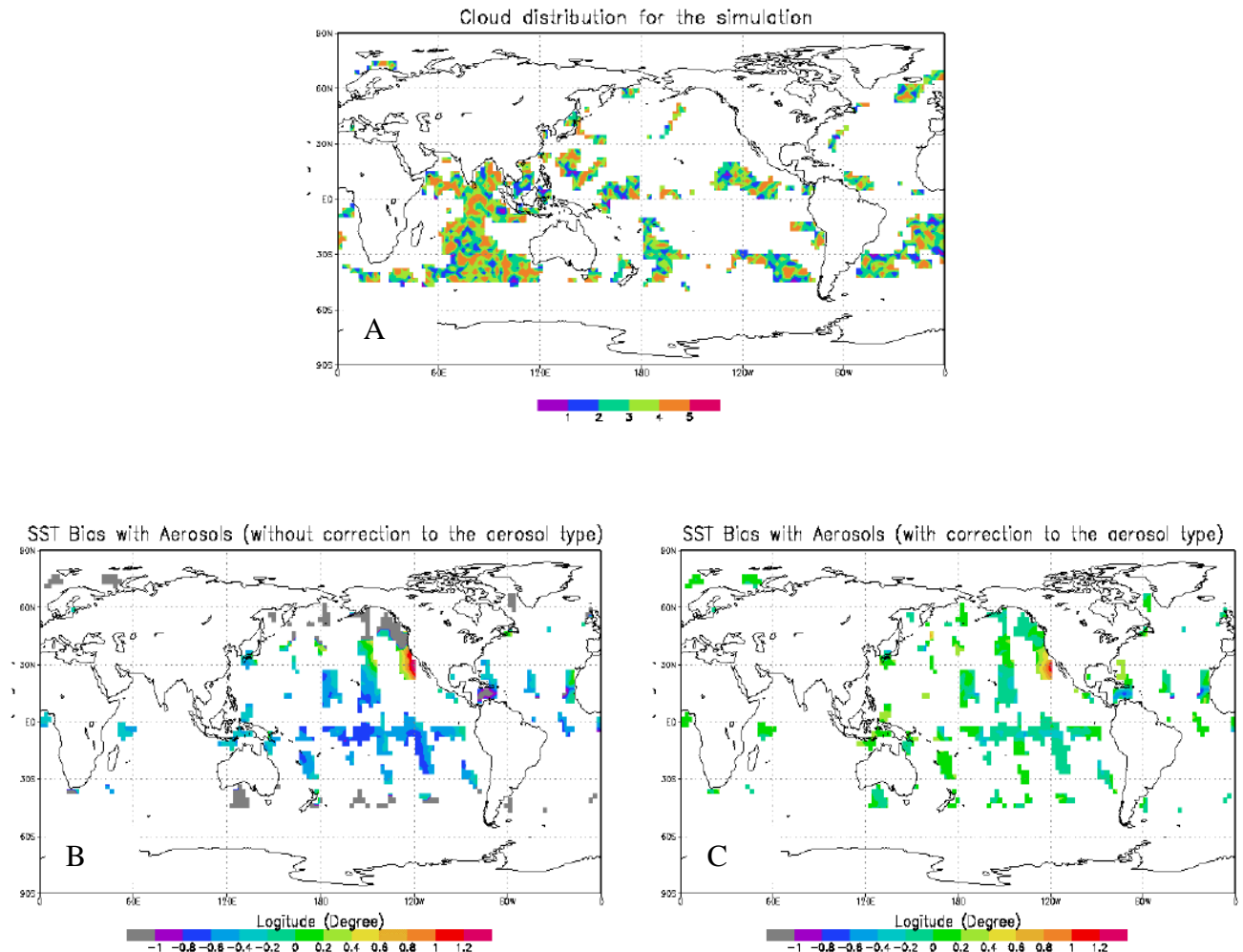


Figure 46. (a) Cloud type distribution in the simulation. (b) SST bias without the consideration of aerosol type. (c) After correction to both of AOT and the aerosol type

4.2.2 Derivation of Bulk SST from Skin SST

The VIIRS SST algorithms for skin and bulk SST are statistical regression retrievals. The algorithms are trained against skin or bulk *in situ* observations to obtain coefficients for the retrievals. Bulk SST may also be derived from skin SST, through the development of an algorithm that describes the bulk-skin temperature difference. Our current architecture supports a simple conversion scheme, and it is extensible to a more complex algorithm.

The bulk-skin temperature difference is subject to both net surface heat flux and the momentum flux (Saunders, 1967). A number of equations have been used to find the bulk-skin temperature difference (e.g., Hasse, 1971, Schluessel *et al.*, 1990). For example, Schluessel *et al.* used following equations to find the ΔT :

Nighttime:

$$\Delta T = a_0 + a_1 u(T_s - T_a) + a_2 u(Q_s - Q_a) + a_3 L \quad (28)$$

Daytime:

$$\Delta T = a_0 + a_1 S / u + a_2 (Q_s - Q_a) + a_3 L \quad (29)$$

where, T_s and T_a are temperatures of surface and air, Q_s and Q_a are water vapor mixing ratios of surface and air, L is the net longwave radiative flux, S the net solar radiative flux, and u the mean wind velocity.

The ΔT can be predicted to an accuracy of approximately 0.2 K provided there are known atmospheric properties. Figure 47 shows the bulk-skin difference from preliminary calculation using NCEP assimilated data. The bulk-skin differences are smaller than 2 K over the region.

The parameters necessary for operational use of a bulk-skin model are available from VIIRS instruments and from auxiliary data sources. Therefore a bulk to skin conversion algorithm could be developed for the VIIRS operational environment.

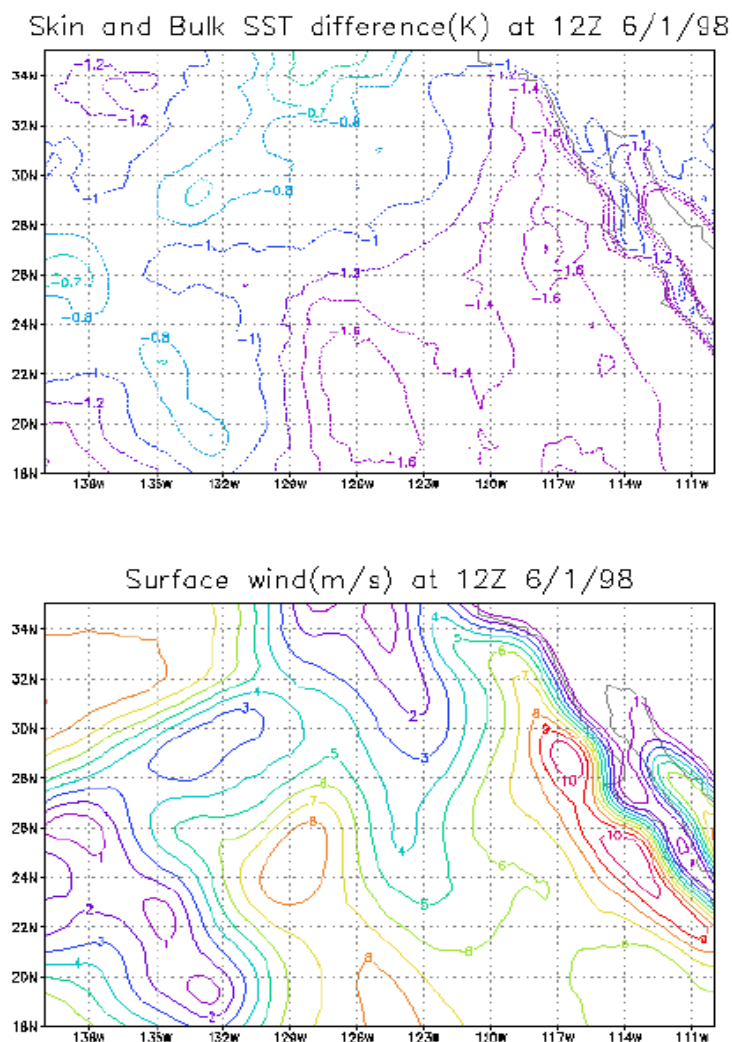


**Figure 47. Bulk-skin SST difference (upper panel),
and the surface wind field at the same time (lower panel).**

4.2.3 Emissivity Correction

As mentioned elsewhere in this document, emissivity of the sea surface is treated as equal to 1, in order to simplify SST retrieval within the constraints of the VIIRS operational timeline. Using this assumption, the VIIRS baseline dual split window algorithm meets requirements under most conditions. However, errors increase at viewing angles greater than 40 degrees, effectively limiting the VIIRS SST retrievals to a 2000 km wide swath. Similarly, high wind conditions can reduce effective emissivity significantly.

While the VIIRS operational timeline does not allow the use of radiative transfer modeling for correction of emissivity, correction factors can be calculated offline and applied to the VIIRS

TOA radiances through the use of LUTs. With appropriate threshold values, this type of correction would not impair the error budget in the central 2000 km of the swath, but would significantly improve the accuracy of SST retrievals at large viewing angles and under high wind conditions.

4.2.4 Iterative Water Vapor Correction

As described in the VIIRS Precipitable Water ATBD [Y3251], the precipitable water algorithm is a five-band derivation of the statistical SST retrieval method. As such, it calculates the effect of precipitable water in each of five MWIR and LWIR bands (3.7, 4.0, 8.6, 10.8, and 12.0 μm).

While the use of an explicit water vapor correction term in the SST retrieval has been suggested (e.g., Emery *et al.*, 1993), errors in PW retrieval have a large impact on the error budget of this form of the SST algorithm. However, if the PW algorithm were subject to the same air mass classification enhancements used in the VIIRS baseline dual split window algorithm, errors in PW retrieval would presumably be reduced. And if the PW retrieval were further tuned to deliver an vapor-only correction to brightness temperatures, the PW retrieval could be employed as a first iteration of the SST retrieval.

An iterative step in the SST retrieval has the potential to improve the accuracy of the retrieval. Since the PW retrieval is already part of the VIIRS operational timeline, this iteration would have little impact on the delivery timeline.

4.2.5 Physical SST Retrieval

Although physical retrievals have not been used for operational SST retrieval due to the large computational requirement and possible instability, they are promising methods for improving the retrieval precision. The ATSR retrieval method is a physically based regression method. This method uses a line-by-line model to simulate the ATSR TOA radiances and incorporates *in situ* skin SSTs with the simulated radiances. This method requires accurate models and highly qualified on-board calibration, as well as very low sensor noise. In order to be useful in an operational setting, sufficient processing power needs to be allocated for the forward modeling. Alternately, it may be possible to develop extensive LUTs for operational use, with those tables populated by offline radiative transfer modeling.

4.2.6 Extended Air Mass Classification

The VIIRS software architecture has been designed to ease the implementation of enhancements using a structure of LUTs for software switches and for algorithm coefficient modifications. Additional modifiers can easily be added, such as the use of brightness temperature differences to select sets of algorithm coefficients, as in the MODIS and AVHRR algorithm design. It is recommended that related VIIRS products, such as the VIIRS cloud, aerosol, and precipitable water products, be studied further for additional air mass classifications that may improve SST retrieval accuracy. Seasonal and meridional trends in error may also be correctable.

5.0 REFERENCES

- Barton, I. J., A. J. Prata, and D. T. Llewellyn-Jones (1993). The Along Track Scanning Radiometer – an Analysis of coincident ship and satellite measurements. *Adv. Space Res.*, 13, 69.
- Berk, A., L. S. Bemstein, and D. C. Robertson (1989). MODTRAN: A moderate resolution model for LOWTRAN 7, Rep. GLTR-89-0122. Burlington, MA: Spectral Sciences, Inc.
- Brown, O. B., and P. J. Minnett (1996). MODIS Infrared Sea Surface Temperature ATBD.
- Cornette, W. M., P. K. Acharya, D. C. Robertson, and G. P. Anderson (1994). Moderate spectral atmospheric radiance and transmittance code (MOSART), Rep. R-057-94 (11-30). La Jolla, CA: Photon Research Associates, Inc.
- Emery, W. J., Y. Yu, G. A. Wick, P. Schluessel, and R. W. Reynolds (1994). Correcting infrared satellite estimates of sea surface temperature for atmospheric water vapor attenuation. *J. Geophys. Res.*, 99, 5219-5236.
- Griggs, M. (1985), A method to correct satellite measurements of sea surface temperature for the effects of atmospheric aerosols. *J. Geophys. Res.*, 90, 12951-12959.
- Hasse, L. (1971). The sea surface temperature derivation and the heat flow at the sea-air interface. *Boundary Layer Meteor.*, 1, 368-379
- Ji, Y., and A. D. Vernekar (1997). Simulation of the Asian summer monsoon of 1987 and 1988 with a regional model nested in a global GCM. *J. Climate*, 10, 1965-1979.
- Kalnay, E., M. Kanamitsu, R. Kistler, W. Collins, D. Deaven, L. Gandin, M. Iredell, S. Saha, G. White, J. Woollen, Y. Zhu, M. Chelliah, W. Ebisuzaki, W. Higgins, J. Janowiak, K. C. Mo, C. Ropelewski, J. Wang, A. Leetmaa, R. Reynolds, R. Jenne, and D. Joseph, 1996: The NMC/NCAR 40-Year Reanalysis Project". *Bull. Amer. Meteor. Soc.*, 77, 437-471.
- Kearns, E. J., J. A. Hanafin, R. Evans, P. J. Minnett, and O. B. Brown, 2000: An independent assessment of Pathfinder AVHRR sea surface temperature accuracy using the Marine--Atmosphere Emitted Radiance Interferometer. Bulletin of the American Meteorological Society. Vol. 81, No. 7, p. 1525-1536.
- Kneizys, F.X., E.P. Shettle, W.O. Gallery, J.H. Chetwynd, L.W., Abreu, J.E.A. Selby, S.A. Clough and R.W. Fenn, "Atmospheric transmittance/radiance: computer code LOWTRAN 6." Air Force Geophysics Laboratory, Report AFGL-TR-83-0187, Hanscom AFB, MA. 1983.
- Kneizys, F. X., E. P. Shettle, L. W. Abreu, J. H. Chetwynd, G. P. Anderson, W. O. Gallery, J. E. A. Selby, and S. A. Clough (1988). Users Guide to LOWTRAN 7, Rep. AFGL-TR-88-0177. Bedford, MA: Air Force Geophys. Lab.

- Legeckis, R., and T. Zhu (1997). Sea surface temperature from the GOES-8 geostationary satellite. *Bull. Amer. Meteor. Soc.*, 78, 1971-1983.
- May, D. A., L. L. Stowe, J. D. Hawkins, and E. P. McClain (1992), A correction for Saharan dust effects on satellite sea surface temperature measurements. *J. Geophys. Res.*, 97, 3611-3619.
- May, D. A., M. M. Parmeter, D. S. Olszewski, and B. D. Mckenzie (1998). Operational processing of satellite sea surface temperature retrievals at the Naval Oceanographic Office. *Bull. Amer. Meteor. Soc.*, 79, 397-407.
- McClain, E. P., W. Pichel, and C. Walton (1985). Comparative performance of AVHRR-based multichannel sea surface temperature. *J. Geophys. Res.*, 89, 11587-11601.
- McClain, E. P., W. G. Pichel, C. C. Walton, Z. Ahmed, and J. Sutton (1983). Multi-channel improvements to satellite derived global sea surface temperatures. Proc. XXIV COSPAR, *Advances Space Res.*, 2(6), 43-47.
- McClain, E. P. (1989). Global sea surface temperature and cloud clearing for aerosol optical depth estimates. *Int. J. Remote Sensing*, 10, 763-769.
- Reynolds, R. W. (1988). A real-time global sea surface temperature analysis. *J. Climate*, 1, 75-86.
- Reynolds, R. W., and T. Smith (1994). Improved global sea surface temperature analysis using optimum interpolation. *J. Climate*, 7, 929-948.
- Saunders, P. (1967). The temperature at the ocean-air interface. *J. Atmos. Sci.*, 24, 269-273.
- Schluessel, P., W. J. Emery, H. Grassl, and T. Mammen (1990). On the bulk-skin temperature differences and its impact on satellite remote sensing of sea surface temperatures. *J. Geophys. Res.*, 95, 13341-13356.
- Závody, A.M; Mutlow, C.T.; Llewellyn-Jones, D.T. (1995) A radiative transfer model for sea surface temperature retrieval for the along-track scanning radiometer. *Journal of Geophysical Research*, 100(C1):937-952